Received: 28 June 2023 | Revised: 22 March 2024 | Accepted: 3 April 2024

DOI: 10.1111/bre.12865

Basin Research IAS EAGE WILEY

RESEARCH ARTICLE

Quantification of sediment fluxes and intermittencies from Oligo–Miocene megafan deposits in the Swiss Molasse basin

Philippos Garefalakis[1] | **Ariel Henrique do Prado**[1] | **Alexander C. Whittaker**[2] | **David Mair**[1] | **Fritz Schlunegger**[1]

[1]Institute of Geological Sciences, University of Bern, Bern, Switzerland

[2]Department of Earth Science and Engineering, Imperial College London, London, UK

Correspondence
Philippos Garefalakis, Institute of Geological Sciences, University of Bern, Baltzerstrasse 1+3, Bern 3012, Switzerland.
Email: philippos.garefalakis@unibe.ch

Funding information
Schweizerischer Nationalfonds zur Förderung der Wissenschaftlichen Forschung

Abstract

The conglomerates preserved in alluvial fans in the Swiss Molasse basin provide crucial insights into the sedimentary dynamics of these routing systems. In particular, the architectural trends and grain sizes of such deposits reveal information on the sediment fluxes and record variations in the intermittency — a proxy for the fan's activity — that indicate on the relative importance of tectonic or climatic controls on sediment production and transport. Here, we calculated intermittencies from sediment transport dynamics using the ratio between the long-term average and the short-term instantaneous unit sediment fluxes during bankfull discharge conditions. For this, we collected grain size data from three palaeo-fan systems that were active through Oligo–Miocene times and that reveal preserved proximal–distal relationships. The three fan systems, which we term the western, central and eastern fans, show significant differences in their long-term sediment budget but equivalent magnitudes of the sediment transport dynamics expressed through the intermittency factor. The eastern fan records a low long-term sediment flux (5.7 km^2 Myr^{-1}), which needed the fan to be active during ca. 8 $h\,yr^{-1}$ (intermittency factor of 0.89 $\times 10^{-3}$). The western fan reveals a higher long-term sediment flux (16.2 km^2 Myr^{-1}), which could have accumulated during ca. 16 $h\,yr^{-1}$ (intermittency factor of 1.83 $\times 10^{-3}$), thereby reflecting a more active system. The central fan records the largest long-term sediment flux (40.3 km^2 Myr^{-1}), where ca. 57 $h\,yr^{-1}$ of sediment transport would be required to deposit the supplied material (intermittency factor of 6.53 $\times 10^{-3}$), thus representing the most active system. By relating these characteristics to the regional exhumation history, we consider that the central fan mainly recorded the transient response of the Alpine surface to the break-off of the European mantle lithosphere slab. Contrarily, the western and eastern fans were formed during the Alpine evolution when steady-state conditions between uplift and erosion were reached and when sediment fluxes to the basin were lower. Despite differences in the tecto-geomorphic and climatic boundary conditions, our data suggest that

these Oligo–Miocene megafans could accomplish their mean annual sediment transport work within a few hours or days per year.

KEYWORDS

alluvial fans, grain size, intermittency, sediment flux, sedimentary dynamics, self-similarity, Swiss Molasse basin

1 | INTRODUCTION

The formation of alluvial fans in sedimentary basins at the tip of an adjacent mountain belt is influenced by either tectonic or climatic perturbations in the source area or adjustments in the eustatic sea level farther down-system (Blair & McPherson, 1994; Harvey et al., 2005; Ventra & Clarke, 2018). Signals of changes in sediment flux and water discharge, propagating from the source area into the sedimentary sink, are considered as indicators of these processes (Allen et al., 2013; Castelltort et al., 2015; Romans et al., 2016). Changes in sediment flux can modify the distribution of the sediment's calibre along alluvial fans in basins (D'Arcy et al., 2017; Flemings & Jordan, 1990; Heller & Paola, 1992; Jordan, 1981; Whittaker et al., 2011), which is further influenced by the spatial distribution of accommodation space, hence controlled by the basin's subsidence (Beaumont, 1981; Brooke et al., 2018; Sinclair et al., 1991; Sinclair & Naylor, 2012). From a stratigraphic perspective, coarse-grained conglomerate beds with sandstone and mudstone interbeds are typically attributed to deposits of alluvial fans, or megafans if their radii exceed >10 km (Allen et al., 1991; Blair & McPherson, 1994; Harvey et al., 2005; Kempf et al., 1999; Matter, 1964; Schlunegger et al., 1996). Consequently, sediment flux signals are often preserved in such stratigraphic records through the arrangement and the size of grains. Information on the small-scale stacking pattern and large-scale architecture of these deposits, coupled with a chronological framework, allows us to quantify sedimentary dynamics on these fans (Allen et al., 2013; Bridge, 1985; Flemings & Jordan, 1989; Heller & Paola, 1992; Ventra & Nichols, 2014). Such stratigraphic sequences have also been identified in the Oligo–Miocene Swiss Molasse basin (SMB), located on the northern margin of the European Central Alps (Figure 1). This basin hosted three major large-scale dispersal systems (i.e. megafans), to which we refer to as the western, the central, and the eastern fans, for simplicity (Section 2.3).

Previous studies have linked changes in the stacking pattern and grain sizes in Molasse conglomerates to orogenic events in the Alpine hinterland (Allen et al., 1991; Garefalakis & Schlunegger, 2018; Schlunegger & Castelltort, 2016; Sissingh, 1997). Some authors provided initial estimates of sediment fluxes, yet at the scale of the entire SMB only. Corresponding results are either based on the preserved mass (Hay et al., 1992) or volume of sediments (Kuhlemann, 2000; Kuhlemann, Frisch, Dunkl, & Székely, 2001; Schlunegger, 1999). Despite differences in the methodological approaches, all studies converge to the notion that sediment fluxes started to increase after 30 Ma, and that this trend persisted throughout the Oligocene, reaching a peak around 20 Ma in Miocene times (22,000 km^3 Myr^{-1}). This was followed by a decline and subsequent short-term increase. Since 16 Ma the fluxes stabilised at lower values (15,000 km^3 Myr^{-1}). However, there exist no estimates of sediment fluxes at the megafan scale in the SMB, nor information on their temporal activity—known as the intermittency. The intermittency factor expresses the proportion of a year during which a system accomplishes its mean annual transport work (Dury, 1961; Mohrig et al., 2000; Navratil et al., 2006; Parker et al., 1998). For the purpose of these calculations, sediment transport capacity at channel forming conditions is typically assumed (Hayden et al., 2021; Lyster et al., 2022). As such, a highly intermittent system experiences occasional sediment transport, whereas a non-intermittent system is characterised by continuous sediment transport (Paola et al., 1992). Intermittent flow or sediment transport is widely recognised in modern rivers but is directly applicable to alluvial fan systems as well (McLeod et al., 2023; Meybeck et al., 2003; Paola et al., 1992; Tucker

Highlights

- We determined sedimentary transport dynamics, expressed as the intermittency, of alluvial fan deposits.
- The fans in the Swiss Molasse accomplished their mean annual sediment transport work in a few hours per year.
- The tecto-geomorphic evolution of the Central Alps largely influenced the formation of the three analysed fans.
- We provide insights in the long-term and instantaneous sediment fluxes at the scale of individual fans.

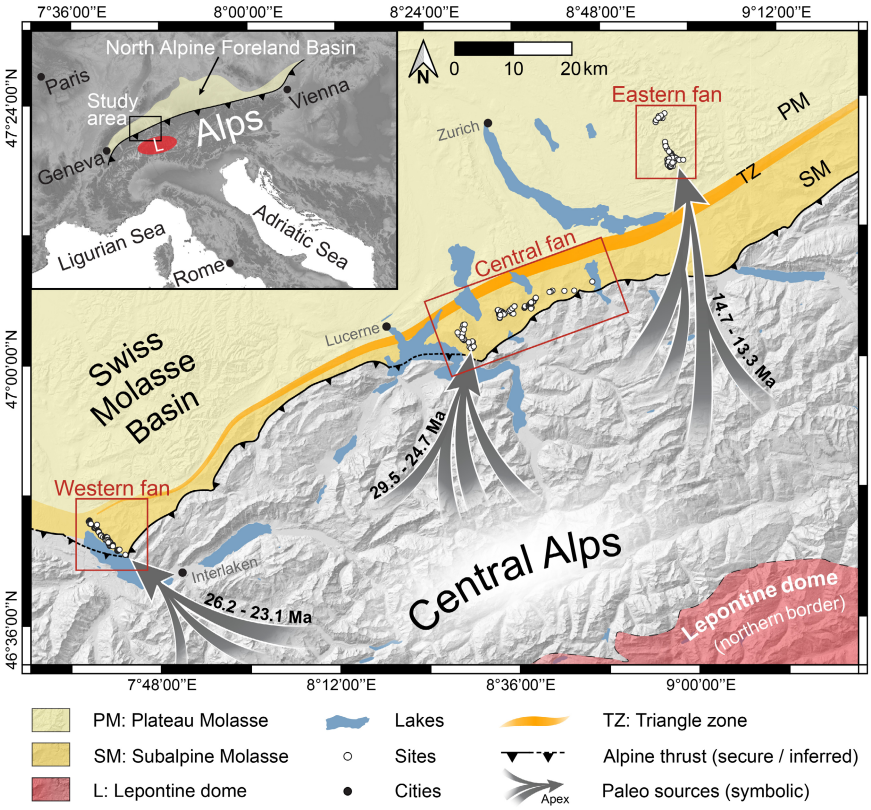

FIGURE 1 Simplified geological map of the Swiss Molasse basin and the location of the three palaeo megafan systems. The three fans were all sourced from the Central Swiss Alps throughout the Oligo- and Miocene. Sites denote locations where grain size data were collected (see also detailed geological maps of each fan system in Appendix I). The underlying digital elevation model (LiDAR DEM Swiss ALTI3D; © swisstopo) shows the current topography of the Alps. The inset map shows the position of the North Alpine Foreland Basin in relation to the Alps and the present-day position of the Lepontine dome (EU-DEM v1.1 © European Union, Copernicus Land Monitoring Service 2023, European Environment Agency, EEA).

& Slingerland, 1997). The intermittency also serves as a measure for the geomorphologic effectiveness of a fluvial system (Hayden et al., 2021; Lyster et al., 2022; Pfeiffer & Finnegan, 2018; Wainwright et al., 2015; Wickert & Schildgen, 2019), for which we consider as a reference a bankfull discharge event during which all grains are transported at nearly the same rate (Paola et al., 1992; Parker et al.,1982; Parker & Toro-Escobar, 2002).

Here, we estimated the long-term and short-term sediment fluxes and particularly the intermittencies of the three major megafan systems in the SMB based on stratigraphic information preserved by well-exposed sections (Figure 1). Our aim is to unravel the activity of these palaeo-fans, mainly because alluvial fan intermittencies are of key importance for determining how these systems record tectonic and climatic signals in the Alpine hinterland. Accordingly, a broader goal of this work is to explore how the erosional–depositional mechanisms responded to the built-up of the Alpine topography, which occurred simultaneously with the construction of the target fans.

2 | GEOLOGICAL SETTING

2.1 | The Central Alps and the SMB

The SMB is located north of the Central Alps and bordered to the South by the basal Alpine thrust (Figure 1). It formed synchronously with the development of the Alps between the Oligocene and Miocene, documenting the erosional response of sediment routing systems to the different stages of the Alpine orogeny and the related topographic evolution (Allen et al., 1991; Beaumont, 1981; Pfiffner, 1986; Schlunegger & Kissling, 2022). The SMB comprises two transgressive–regressive mega-cycles, each characterised by (shallow) marine and freshwater deposits (Kuhlemann & Kempf, 2002; Matter et al., 1980). The Molasse basin is further divided into the undeformed and flat-lying Plateau Molasse, constituting the largest portion of the SMB, and the tilted, folded and thrusted Subalpine Molasse situated at the Alpine border farther to the South (Figure 1). Terrestrial clastic sedimentation is recorded by the Freshwater Molasse, which sedimentation occurred through transverse braided systems on alluvial megafans near the Alpine front (Bürgisser, 1981; Kempf & Matter, 1999; Matter et al., 1980; Schlunegger et al., 1996; Stürm, 1973). The Freshwater type of Molasse sedimentation led to the formation of stratigraphic deposits that have been extensively analysed for their sedimentological properties and ages (Kempf & Pfiffner, 2004; Matter & Weidmann, 1992; Schlunegger et al., 1993; Schlunegger, Jordan, et al., 1997). In addition, petrological and geochemical analyses of individual clasts and the grain-supporting matrix resulted in a detailed knowledge about the provenance and the

source-to-sink routing of the clastic material (Anfinson et al., 2020; Bolliger, 1998; Büchi, 1958; Bürgisser, 1981; Eynatten, 2003; Kempf et al., 1999; Matter et al., 1980; Schlunegger, Jordan, et al., 1997; Spiegel et al., 2000; Stürm, 1973; Tanner, 1944; van der Boon et al., 2018).

2.2 | Orogenic evolution and climatic conditions during the Oligo–Miocene

The three target fans were active during the Oligo- and Miocene, reflecting the erosional evolution of the adjacent Central Alps (Kuhlemann, 2007; Pfiffner, 1986; Schlunegger et al., 1998). In the Oligocene, between 32 and 26 Ma, the Central Alps underwent significant topographic modifications due to rapid uplift, particularly in the Lepontine area (Figure 1; Steck et al., 2013), expressed by high exhumation rates (Boston et al., 2017; Schlunegger & Willett, 1999) and substantial sediment fluxes to the basin (Kuhlemann, Frisch, Dunkl, & Székely, 2001). These tectonic adjustments have been explained either by crustal thickening resulting from a northward thrusting of the Alpine orogen (Beaumont et al., 1996; Pfiffner et al., 2002; Schmid et al., 1996) or by a slab break-off occurring at 32–30 Ma (Kästle et al., 2020; Schlunegger & Castelltort, 2016; Schlunegger & Kissling, 2022; Sinclair, 1997). The uplift related to slab break-off initiated a transient stage in the evolution of the Alpine landscape (Garefalakis & Schlunegger, 2018), resulting in a highly dissected terrain formed through the headward retreat of the erosional front, thereby exhuming the crystalline core of the Alps at that time. This adjustment to high uplift in the Lepontine area persisted until 25–24 Ma, when the Alps reached a steady-state topography (Schlunegger & Kissling, 2015). In the Miocene, around 22–20 Ma, changes occurred in the Alpine hinterland when the exhumation of the external crystalline massifs was initiated and when tectonic unroofing in the area surrounding the Lepontine Dome (Figure 1) reached the highest rate (Baran et al., 2014; Boston et al., 2017; Herwegh et al., 2017; Schlunegger & Norton, 2013). This induced a re-organisation of the drainage network in the core of the Alps, where the drainage network evolved from an orogen-normal oriented system with short streams and steep gradients (Figure 2a) to an orogen-parallel oriented system with longer flow paths and shallower gradients (Figure 2b; Schlunegger et al., 1998; Kühni & Pfiffner, 2001; Spiegel et al., 2001; Stutenbecker et al., 2019; Bernard et al., 2021). As a consequence, the supply of sediment to the SMB decreased (Hay et al., 1992; Kuhlemann, Frisch, Dunkl, Székely, & Spiegel, 2001; Schlunegger, 1999). Also around 20 Ma, syn-depositional back-thrusting along the southern margin of the Plateau Molasse resulted in the establishment of the Triangle Zone (Figure 1; Kempf et al., 1999; Schlunegger & Mosar, 2011) and the formation of a basin-wide progressive unconformity close to the Alpine thrust front (Schlunegger, Leu, et al., 1997). After a short period of high sediment delivery to the Molasse basin between 18 and 16 Ma, the supply rates of clastic material continuously decreased (Kuhlemann, Frisch, Dunkl, Székely, & Spiegel, 2001).

From a palaeoclimate perspective, stable carbon and oxygen isotope data collected in the Molasse basin from Chattian deposits (Late Oligocene) indicated that around 25.5 Ma of the palaeoclimate possibly changed from a humid to a warmer and drier, but probably stormier (Schlunegger & Norton, 2013) climate (Berger, 1992; Kuhlemann & Kempf, 2002; Schlunegger et al., 2001; Schlunegger & Castelltort, 2016). In the Miocene, remnants of floral faunas (Mosbrugger et al., 2005) and data of carbon and oxygen isotope collected from pedogenic carbonates (Krsnik et al., 2021; Methner et al., 2020) suggest a cooling event between 15 and 14 Ma, immediately following the mid-Miocene Climatic Optimum (around 17 Ma). These changes were also interpreted to have occurred globally (Zachos et al., 2001).

2.3 | Temporal and spatial framework of the target fans

The fan deposits have been placed into a chronological framework using magnetopolarity stratigraphies paired with micro-mammalian data collected along stratigraphic sections (Kälin & Kempf, 2009; Kempf et al., 1997; Schlunegger, Leu, et al., 1997). The westernmost section in the study area (western fan, Figure 1), known as the Thun-section, and its contemporaneous twin-section located farther to the East–northeast, recorded the construction of the Blueme megafan during Oligocene times between 26.2 and 23.1 Ma (Schlunegger et al., 1993, 1996; Strasky et al., 2022). In the central part of the SMB (central fan, Figure 1), the Rigi megafan constitutes another major depositional system, which was active 29.5–24.7 Ma ago (Schlunegger, Jordan, et al., 1997; Schlunegger, Matter, et al., 1997). Contemporaneous deposits farther downstream are encountered at four sections situated at the proximal basin border (Schlunegger, Jordan, et al., 1997; Stürm, 1973). In the eastern part of the SMB (eastern fan, Figure 1), deposits of the Hoernli megafan are exposed along two stratigraphic sections recording the evolution of this dispersal system (Büchi, 1958; Bürgisser, 1981; Kälin & Kempf, 2009; Kempf et al., 1997; Kempf & Matter, 1999). These deposits are younger and span the time interval between 14.7 and 13.3 Ma (Kälin & Kempf, 2009; Kempf et al., 1997; Kempf & Matter, 1999). Detailed geological

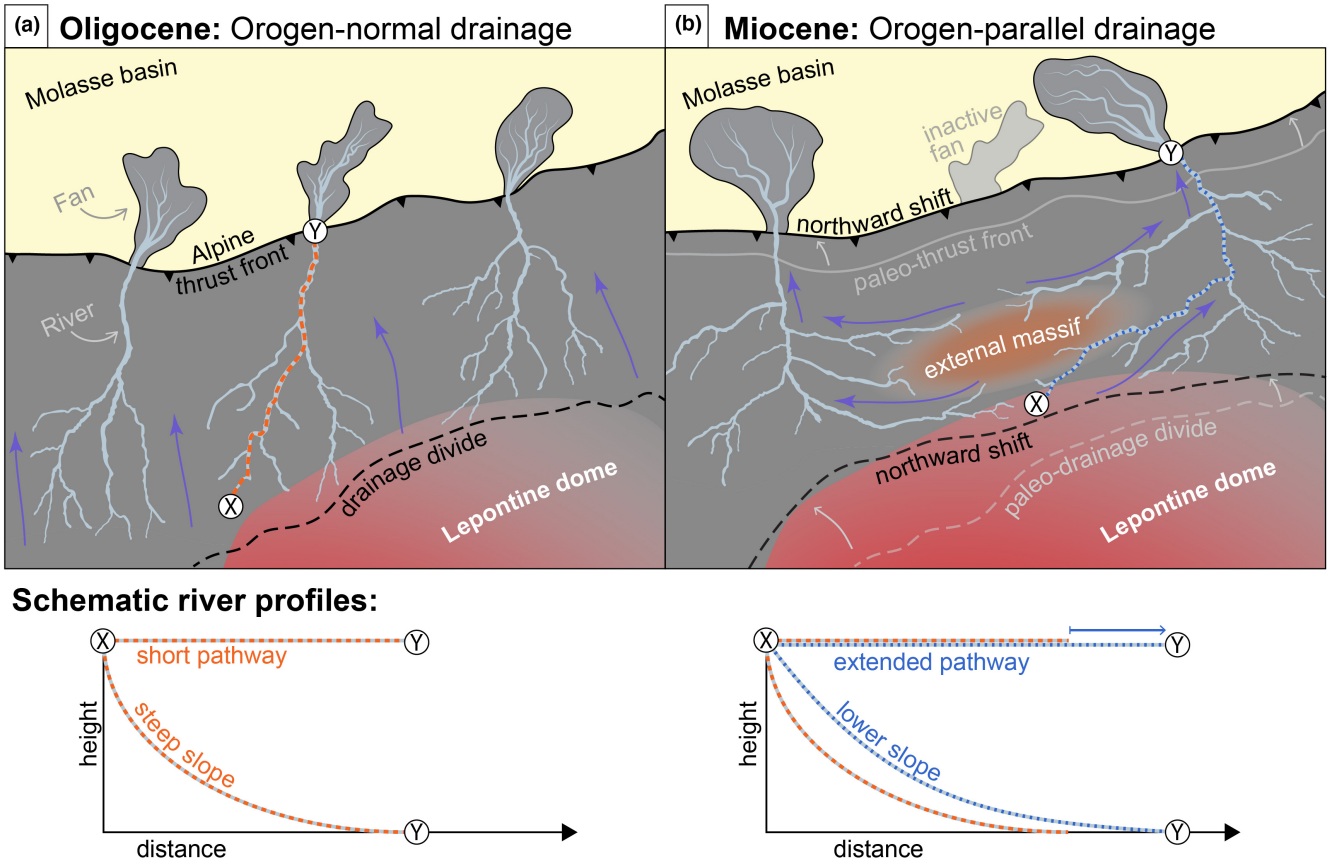

FIGURE 2 Simplified palaeogeographical sketch of the drainage network in the Central Alps and the alluvial fans in the adjacent Molasse basin. (a) During the Oligocene a drainage network, oriented normal to the Alpine strike, originated in the Central Alps (e.g. Kühni & Pfiffner, 2001; Stutenbecker et al., 2019). (b) During the Miocene the drainage network evolved into an orogen-parallel oriented pattern, possibly influenced by the exhumation of the external massifs in the Central Alps and a northward shift of the drainage divide (e.g. Bernard et al., 2021; Schlunegger et al., 1998). This induced a re-organisation of the drainage network that experienced an extension of the pathways and a lowering of the channel slopes respectively (e.g. Schlunegger, 1999; Spiegel et al., 2001).

maps and stratigraphic sections of the three fans are available in Appendix I.

Proximal–distal relationships have been previously reconstructed based on palaeo-flow and petrographic data (Bürgisser, 1981; Garefalakis & Schlunegger, 2018; Kempf et al., 1997; Kempf & Matter, 1999; Schlunegger et al., 1993, 1996; Schlunegger, Jordan, et al., 1997; Stürm, 1973). The position of the palaeo-fan apex was determined through mapping, palaeo-stratigraphic restorations and measurements of discharge directions (details in Appendix I). For modelling purposes, we positioned the apex +3 km upstream of the most proximal location currently exposing the most proximal deposits. This is to compensate for the amount of tectonic erosion during the emplacement of overlying thrust nappes (Pfiffner, 1986), aligning with studies providing relatively precise positions for the palaeo-apex of the western (Schlunegger et al., 1993, 1996) and central fans (Schlunegger, Jordan, et al., 1997; Schlunegger, Leu, et al., 1997; Stürm, 1973). However, the situation is different for the eastern fan, as large parts are not preserved (Bürgisser, 1980, 1981; Bolliger, 1998) due to basin inversion and erosion of the Molasse sediments since the Pliocene at the latest (Cederbom et al., 2011; Mazurek et al., 2006; Schlunegger & Mosar, 2011). Consequently, the position of the palaeo-apex of the eastern fan may have been located at least +3 km upstream, or possibly even ca. +10–15 km farther to the Southeast according to Bürgisser (1981, 1980). In this context, we investigated the sensitivity of the palaeo-apex' position on the outcomes of the grain size fining model (details in Appendix I.c). Accordingly, the distance between the palaeo-apex and the most distal location is approximately 12 km for the western, 12 versus 24 km for the eastern, and 32 km for the central fan.

From a sedimentological and stratigraphic perspective, the analysed deposits exhibit similar large-scale architectures (Figure 3). Proximal locations display sequences characterised by hundreds of m-thick amalgamations of conglomerate beds, each several dm- to m-thick, intercalated by sandstone and mudstone beds of

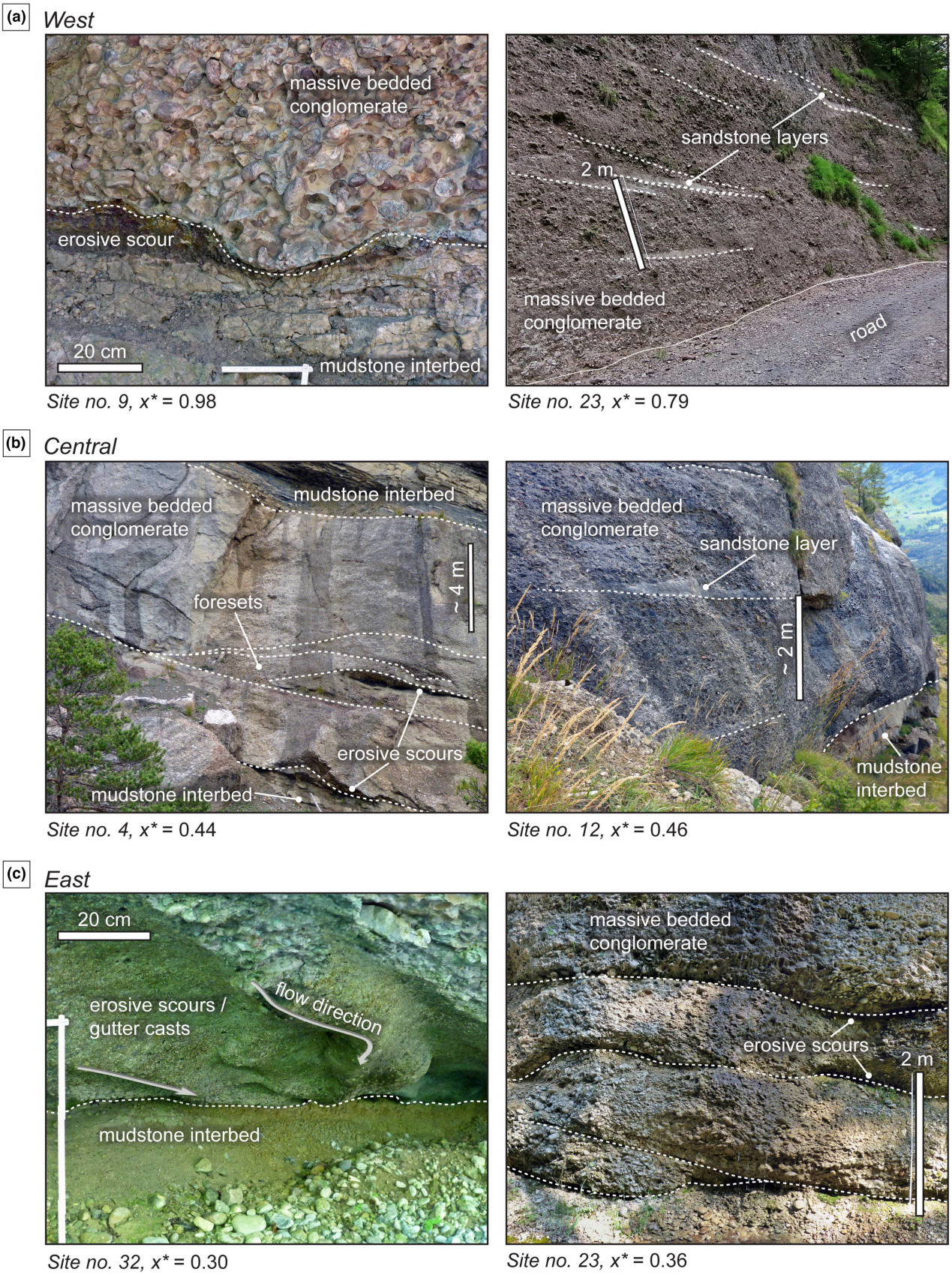

FIGURE 3 Field examples of outcrops showing conglomerate beds and sedimentary structures of the (a) western, (b) central and (c) eastern fan systems. See Appendix I for the locations of these sites.

a few m-thickness. Towards more distal positions along each palaeo-fan, individual conglomerate beds thicken to a few meters and amalgamations become rare, while the occurrence of m-thick sandstone and mudstone interbeds increases. This signifies a downstream transition from a stream featuring braided, shallow channels to an environment with single-thread and deep channels (Boothroyd & Ashley, 1975; Church, 2006; Garefalakis & Schlunegger, 2018; Huggenberger & Regli, 2009). At distal positions, mudstones showing reddish to yellow mottling, rootlets and pedogenic carbonate nodules are interpreted as deposits on floodplains bordering the channel belts (Garefalakis & Schlunegger, 2018; Kempf et al., 1999; Schlunegger et al., 1993; Schlunegger, Jordan, et al., 1997; Stürm, 1973).

3 | METHODS

3.1 | Revision of the chronological framework

Published magnetostratigraphic data were re-calibrated by correlations with the recent Global Time Scale GTS2020 (Gradstein et al., 2020) and integrations of new mapping outcomes (Hantke et al., 2022; Strasky et al., 2022) to establish an updated chronological and sedimentological framework. This revision was necessary because the original temporal calibrations of the sections were based on correlations of the magnetostratigraphic framework with either the CK95 (Cande & Kent, 1995) or the ATNTS2004 time scales (Lourens et al., 2004). However, these chronologies have partially different numerical ages than the GTS2020, particularly for the timescales of interest. The detailed chronostratigraphic revision is given in Appendix I.

3.2 | Intermittency

We used the ratio between the long-term sediment flux $Q_{s_A}^*$ and the instantaneous bankfull bedload flux Q_b* as a proxy for the intermittency of our target palaeo-fans (Hayden et al., 2021; Lyster et al., 2022; Paola et al., 1992). The dimensionless intermittency factor (I_F) is calculated as:

$$I_F = Q_{s_A}^* / Q_b^* \, [-] \quad (1)$$

Here, $Q_{s_A}^*$ represents the sediment flux that was necessary to build up the stratigraphic sections of the analysed fan deposits. This value was computed with the grain size fining model (Section 3.3). Q_b* is the theoretical sediment flux that can be sustained during bankfull conditions, and calculated with the Meyer-Peter and Müller (1948) bedload equation (MPM-equation; Section 3.4). Hence, the ratio between $Q_{s_A}^*$ and Q_b* signifies the fraction of a year during which a system accomplishes its average annual transport work if bankfull transport is maintained (see also Introduction). We also expressed the I_F as the (system's) activity in hours per year [h yr^{-1}].

3.3 | Long-term sediment flux

3.3.1 | Principles and basic equations

Long-term sediment fluxes were calculated by applying the self-similar grain size fining model (see for details on the model Appendix II) for gravel introduced by Fedele and Paola (2007). The model depends on input parameters that can be derived directly from field observations. These are: (i) the down-system length of the depositional system, (ii) the spatial distribution of accommodation space and its down-system decreasing rate and (iii) the grain size distribution at the apex. We then iteratively determined (through the grain size fining model) the sediment flux at the fans' apex, which corresponds to the long-term sediment flux $Q_{s_A}^*$. The model is ultimately derived from the Exner-equation (Fedele & Paola, 2007; Paola & Voller, 2005). It is based on the principle that deposition or erosion of sediment results in a modification of the bed elevation, which itself changes in proportion to the volume of the deposited or eroded mass (Paola & Voller, 2005). Thus, it is founded on a mass-conserving sorting process (Fedele & Paola, 2007) where the balance between sediment being deposited, transported or bypassed is maintained at any point on the fan (Allen et al., 2013; Armitage et al., 2011; Brooke et al., 2018; Duller et al., 2010; Fedele & Paola, 2007). Additionally, it assumes that gravel grain size distributions are self-similar (i.e. the mean and standard deviation decrease down-system at the same rate). In its simplest form the model computes the spatial distribution of sediment flux $Qs^*(x^*)$ through:

$$Q_s^*(x^*) = Q_{s_A}^* - (1 - \lambda_p) \int_0^L r^*(x^*)\, dx^* \left[m^3\, Myr^{-1}\, m^{-1}\right] \quad (2)$$

Here, $Q_{s_A}^*$ is the unit input sediment flux at the system's apex ($x^*=0$, where x^* is the downstream length normalised by the total depositional length L, i.e. $x^*=x/L$), $\lambda_p=0.3$ is the sediment porosity and set as constant (Fedele & Paola, 2007) and r^* is the subsidence rate along distance (Equation 7 and Section 3.3.3). Following a dimensionless distance transformation (i.e. y^*, Equation (S7) in Appendix II) applied to the spatial distribution

of sediment mass (i.e. Equation (S4) in Appendix II) and considering the principle of self-similarity (Equation 5, see next), the modelled grain size D_m along distance is calculated through:

$$D_m(x^*) = D_A + \varphi_A \frac{C_2}{C_1}\left(exp^{-C_1 y^*} - 1\right)\,[m] \qquad (3)$$

Here, D_A is the input grain size, calculated through Equation (8), and φ_A its uncertainty, both at the apex ($x^*=0$). We expressed φ_A as the product of D_A and the coefficient of variation, C_v, thereby following D'Arcy et al. (2017). The constants C_1 and C_2 describe how the variance in sediment supply is partitioned in downstream variations of the mean grain size (C_2) and in variations of its standard deviation at a specific site (C_1). The ratio of C_1 and C_2 can be expressed by C_v (Fedele & Paola, 2007) and thus by the ratio between the standard deviation and the mean of the grain size data $\left(C_v = \sigma / \overline{D}\right)$. By modelling the spatial distribution of sediment, we also calculated the ratio between the volumes of sediment that was supplied to the system and deposited on the fan as a function of the available accommodation space. This ratio (>1: overfilled; <1: underfilled basin) is expressed as F_E, which is the fraction of sediment in excess (D'Arcy et al., 2017):

$$F_E = \frac{Q_{s_A}^*}{\left(1-\lambda_p\right)\int_0^L r^*(x^*)\,dx^*}\,[-] \qquad (4)$$

As we noted earlier, the model assumes that grain sizes fine downstream in a self-similar way. Accordingly, the distribution of the grain size similarity variable ξ (Brooke et al., 2018; Fedele & Paola, 2007) for each site is expressed through:

$$\xi = \frac{D_k - \overline{D}}{\sigma}\,[-] \qquad (5)$$

The distribution of this variable should approximately remain similar at any downstream position of a fluvial system. Here, D_k is the size of an individual grain measured at a given location, and $\overline{D}$ and σ are the mean and standard deviation of the grain size distribution at that site. For each fan, we statistically compared the ξ distributions of all sites using the Kolmogorov–Smirnov two-sample (hereafter KS2) test (Hodges, 1958). We tested the null hypothesis H_0 that two ξ distributions of two locations are similar and likely drawn from identical distributions at a significance level of alpha = 0.05 (i.e. 95% confidence interval; two samples are statistically similar if the reported $p > 0.05$).

3.3.2 | Adjustments of the grain size fining model

We applied a bootstrapping to recover possible input unit sediment fluxes and iteratively adjusted $Q_{S_A}^*$ (Equation 2 before) through obtaining the best fit between the results of the modelled grain sizes (Equation 3 before) and the grain size data collected in the field (Section 3.3.3.). Specifically, we calculated the mean absolute error (MAE) thereby quantifying the absolute average magnitude of errors between the grain size data collected at outcrops in the field (i.e. D_{50}, see also Section 3.3.3) and the modelled grain size values D_m. Conceptually, if D_m is generally larger than the D_{50}, and in order to minimise the MAE, then the input sediment flux was decreased by an increment of $Q_{S_A}^* \cdot 0.1$; if the opposite was the case, then the input sediment flux was increased by steps of $Q_{S_A}^* \cdot 0.1$:

$$if\, D_m(x^*)\,[m] \begin{cases} > D_{50}(x^*)\,[m] \rightarrow Q_{s_A}^* - Q_{s_A}^* \bullet 0.1\,\left[km^2\,Myr^{-1}\right] \\ < D_{50}(x^*)\,[m] \rightarrow Q_{s_A}^* + Q_{s_A}^* \bullet 0.1\,\left[km^2\,Myr^{-1}\right] \end{cases} \qquad (6)$$

Here, D_m is the modelled grain size calculated through Equation (3) and D_{50} is the 50th grain size percentile (Section 3.3.3), both along downstream distance (x^*), and $Q_{S_A}^*$ is the input unit sediment flux in [km^2 Myr^{-1}]. We repeated this procedure for each of the 10^4 possibilities resulting from the bootstrapping until the MAE was minimised for each iteration. In addition, for a given iteration we kept all other parameters (i.e. D_A, φ_A, C_v, C_1, C_2, and r^*, see equations before and Section 3.3.3) fixed and only adjusted the input sediment flux $Q_{S_A}^*$.

3.3.3 | Field data: Subsidence rates and grain size

Equation (2) requires information on the subsidence rates as input parameter. We determined these rates using information on the preserved thickness of the sedimentary units and the time interval during which they were deposited (see Appendix I for details). We then approximated the subsidence rates along a transect down the palaeo-fan by an exponential function (D'Arcy et al., 2017; Duller et al., 2010; Sinclair & Naylor, 2012; Whittaker et al., 2011):

$$r^*(x^*) = r_A\, exp^{-\beta(x^*)}\,\left[m\,Myr^{-1}\right] \qquad (7)$$

Here, r_A is the subsidence rate at the apex ($x^*=0$) and β is the rate at which r^* decreases down-system. The resulting exponential decrease of the inferred subsidence rates are typical for a foreland basin setting

(Allen et al., 1991; Sinclair & Naylor, 2012). For each fan, the subsidence pattern relies on data from two (for the western and eastern fans) and four (for the central fan) stratigraphic sections documenting the same sedimentary units along distance (Appendix I). The interpolation between the sections and the extrapolation towards the apex (r_A) were performed through a regression using Equation (7). We additionally calculated the cross-sectional area of the accommodation space (generated through subsidence) along the transect in 2D using the trapezoidal rule. We acknowledge that more detailed estimates of subsidence rates, as for example demonstrated by Armitage et al. (2015), might provide more nuanced insights into the pattern at which sediment was distributed in the basin. In the study area, patterns of sediment distribution assuming down-system stepwise changes in subsidence rates could only have been accomplished by syn-sedimentary faulting, as documented elsewhere by Pfiffner (1986) based on restored sections through the proximal Molasse. Yet, related evidence has not been presented for our study area, so we make the conservative assumption that subsidence rates decreased exponentially down-system, consistent with previous regional work (Allen et al., 2013; Kempf et al., 1999; Schlunegger Jordan, et al., 1997).

Estimates of the long-term sediment fluxes also hinge on the sizes of grains, which we measured on digital photos. Accordingly, for each fan and accessible outcrops (>5 m^2), we captured 3–6 photos using a hand-held camera (Panasonic Lumix FT-5) at a distance of 1–1.5 m from the outcrops. We added a digital grid scaled to the meters stick in the photograph and measured the longest visible axis of 100 grains >2 mm that are situated beneath each grid-node following Wolman (1954) and the protocol of Garefalakis et al. (2023). The resulting grain size distribution at each outcrop is presented using the value of the median or D_{50} grain size percentile, thus the grain size where 50% of the grains are smaller or equal to this specific size. The downstream decrease in grain size has been demonstrated to follow an exponential function (Blom et al., 2016; Litty et al., 2017; Rice, 1999; Sternberg, 1875). Therefore, we approximated fining rates by fitting an exponential regression to the D_{50} of each outcrop, thereby applying the 'Sternberg law' (Sternberg, 1875):

$$D(x^*) = D_A \, exp^{-\alpha(x^*)} \, [m] \tag{8}$$

Here, D_A is the input grain size at the apex ($x^* = 0$), needed as an input parameter of the model, and α is the grain size fining rate along normalised distance x^*, which can also be expressed in [% km^{-1}] (Parsons et al., 2012).

As will be shown, some of the analysed systems show a downstream trend in grain size, yet all fan systems display a large scatter of the D_{50} at some positions – an issue which has been documented in other (palaeo-) alluvial fan systems (e.g. Brooke et al., 2018; Duller et al., 2010). While material supply from tributary sources could explain this variation (Harries et al., 2018; Rice, 1999), we exclude this possibility. Indeed, available information about the heavy mineral and clast compositions suggest that all systems were most likely fed by one feeder channel only (Stürm, 1973; Bürgisser, 1981; Schlunegger et al., 1993; Schlunegger, Jordan, et al., 1997; Kempf et al., 1999; Appendix I). Therefore, the scatter in the stratigraphic grain size data is likely to result from the random selection of sampling sites from the time-integrated deposits of palaeo-alluvial megafans, an important challenge to address when working with stratigraphic archives (Duller et al., 2010; Straub et al., 2020) where we require constraints on the average deposit grain size down-system. Yet despite the scatter of the raw grain size data, fining trends are observable across some of the analysed fans (see Section 4.2). This becomes better visible upon binning the data, where each bin accounts for 25% of the data along the palaeofan transect with equally weighted bins. We justify this binning approach to account for a potential bias related to our sampling technique as outlined earlier, but we still run the model using the un-binned (raw) grain size datasets for the sake of completeness.

3.3.4 | Sensitivity, assumptions and limitations of the grain size fining model

The model is designed for applications to fluvial successions in stratigraphy covering geological timescales of 10^4–10^6 years (Armitage et al., 2011; Duller et al., 2010; Parsons et al., 2012), aligning well with our study objectives. Also for these long timescales, e.g., Duller et al. (2010) identified a direct relationship between the input sediment flux, the formation rate of accommodation space and the rates at which the sediment is distributed along the system (illustrative in Figure 1 of Parsons et al., 2012). Specifically, a constant flux of sediment supplied into a basin would result in a downstream fining over a long distance (low rates of α in Equation 8), if paired with slow rates at which the subsidence decreases in the downstream direction (β in Equation 7). In contrast, grain sizes would rapidly fine over short distances (large α) if the downstream decreasing rate of the underlying subsidence is high (Duller et al., 2010; Flemings & Jordan, 1989, 1990; Parsons et al., 2012; Whittaker et al., 2011). Hence, the grain size fining rate depends

on the spatial distribution of subsidence, and contrariwise, these downstream grain size fining trends can be used to quantify the rates at which sediment was supplied to the basin. The model incorporates these principles (e.g. Equation (S4) in Appendix II). Furthermore, similarities or differences between the three variables (grain size fining rate, spatial distribution of subsidence and input sediment flux) yield first-order inferences on the mechanisms that drive fan formation, and if they are controlled either by a tectonic driving force such as subsidence or by environmental conditions expressed by a large sediment supply.

The grain size fining model is based on specific assumptions and requirements (Duller et al., 2010; Fedele & Paola, 2007; Whittaker et al., 2011) that govern its applicability. It assumes the fluvial system to be entirely depositional at any down-system location, and it hinges on the assumption of unimodal and self-similar grain size distributions. The model only considers selective transport and deposition of coarse-grained material, assuming that streamflow processes are the predominant sediment transport mechanisms. Notably, effects related to abrasion, chemical dissolution or mechanical particle breakdown are neglectable at the scale of alluvial fans (Duller et al., 2010; Ferguson et al., 1996; Hoey & Bluck, 1999; Miller et al., 2014; Parker, 1991; Stock et al., 2008). Exceptions are the headwaters of a stream where gradients are $>0.1\,m\,m^{-1}$ (Miller et al., 2014; i.e. c. 5.7°), which, however, is much steeper than the surface slope of <1° on the target fans (Figure S7 in Appendix V; Schlunegger & Norton, 2013; Garefalakis & Schlunegger, 2018). While some recent modifications of this type of model account for lateral sediment input by tributaries (e.g. Harries et al., 2019) and predict the dispersion of the sediment across a fan in three dimensions (D'Arcy et al., 2017), we opted for a two-dimensional model with material supplied by one feeder channel at the fan's apex (e.g. Duller et al., 2010; Whittaker et al., 2011) due to the absence of evidence for sediment supply by tributaries (see also Appendix I) and the lack of direct constraints on the fan widths.

Note that although this approach has been successfully applied in previous studies (references before and Appendix II), it is important to note its limitations. In particular, the calculations of the long-term sediment flux do capture average budgets on a million-year scale thereby reflecting shifts in tectonically induced processes (e.g. uplift or subsidence) or longer--term environmental controls (e.g. climate shifts) (Allen et al., 2013; Paola & Voller, 2005; Sadler, 1981). Processes occurring at shorter intervals, such as the dynamic formation of channels influencing local bed elevation, are therefore neglected at such timescales (Duller et al., 2010; Harries et al., 2019). However, these variations are important for the calculations of the instantaneous bedload fluxes (see Section 3.4) and thus at a smaller (temporal) scale (Benavides et al., 2022; Lyster et al., 2022; Wainwright et al., 2015).

3.4 | Instantaneous bankfull sediment flux

Bankfull sediment fluxes, or bedload (material >2 mm) sediment transport rates per unit time and width, were calculated using a derivative of the Meyer-Peter and Müller (1948) bedload transport equation (MPM equation; details in Appendix III):

$$Q_b^* = 3.97\left[(1.0+\varepsilon)\,\tau_c^* - \tau_c^*\right]^{1.5}\left(G_S\,g\,{D_{50}}^3\right)^{0.5}\left[m^3\,s^{-1}\,m^{-1}\right]. \quad (9)$$

Here, the constant 3.97 is based on an enhanced and corrected statistical fit (Wong & Parker, 2006) to the original data of Meyer-Peter and Müller (1948), g is the gravitational acceleration ($=9.81\,m\,s^{-2}$) and G_S is the submerged specific gravity, calculated as $[(\rho_s/\rho_w) - 1] = 1.65$, with $\rho_s = 2650\,kg\,m^{-3}$ and $\rho_w = 1000\,kg\,m^{-3}$, for the sediment and water densities respectively. Furthermore, ε is a factor to account for lateral bank erosion (Paola & Mohrig, 1996; Parker, 1978), τ_c^* is the dimensionless critical Shields parameter (Shields, 1936) and D_{50} is the grain size percentile. For τ_c^* we selected values that are uniformly distributed between 0.039 and 0.054 (Julien, 2010), thereby considering various conditions influencing the incipient motion of grains with different sizes (Julien, 2010). The theoretically derived variable ε was initially set to 0.2 (Parker, 1978), but Paola and Mohrig (1996) found $\varepsilon = 0.4$ is more appropriate for calculations of palaeo-hydraulics. For conservative reasons, we applied uniformly distributed values between $\varepsilon = 0.2$ and 0.4 for our calculations. For the estimates of bedload sediment fluxes we solely used the D_{50}, first to account for the conditions during equal mobility of all grains in a channel (Paola & Mohrig, 1996; Wickert & Schildgen, 2019), and second because the MPM equation was calibrated using the D_{50}. As a consequence, any incipient motion of grains smaller than the D_{50} (that would occur prior to the movement of this percentile) is neglected (Recking et al., 2012), which is considered acceptable (Paola & Mohrig, 1996). Note that we are left with a two-dimensional solution due to the lack of channel width estimates. Note also that bedload sediment fluxes calculated through a shear-stress approach are dependent on the competence of a river, which is a function of water depth and channel slope (details in Appendices III and V).

3.5 | Uncertainties and error estimations

We estimated uncertainties using bootstrapping (re-sampling with replacement; 10^4 iterations), which we combined with a Monte Carlo framework where applicable (Garefalakis et al., 2023; Mair et al., 2022; Rice & Church, 1996). Each reported outcome includes either the mean or median value (as indicated) along with the 95% confidence interval (CI) in squared brackets. For example, for the grain size data, we re-sampled 100 grain size values D_k (measured on the photographs, Section 3.3.3) and determined the uncertainties on the D_{50} within the 95% CI. For a median grain size value, this would be expressed as e.g. $D_{50} = 22$ [17–25] mm. Further information on the uncertainties of other parameters is provided in Appendix IV.

4 | RESULTS

4.1 | Sediment accumulation and subsidence rates

At proximal positions on the western fan, 3250 ± 50 m of sediments accumulated between 24.8 and 23.1 ± 0.1 Ma (Thun Lakeside; Figure S1, Appendix I.a), yielding an accumulation rate of 1910 ± 140 m Myr^{-1} (i.e. Thun in Figure 4a). At more distal locations farther to the East–northeast (Praesserebach twin-section; Figure S1, Appendix I), the same sedimentary unit is 1250 ± 50 m thick and was deposited between 24.8 and 24.0 ± 0.1 Ma, yielding a sediment accumulation rate of 1600 ± 260 m Myr^{-1} (Figure 4a) Accordingly, at the apex of the western fan, the median subsidence rate was 2088 [1798–2477] m Myr^{-1}, from where the subsidence rates decreased in the downstream direction at a median rate of 2.93 [−0.03–6.92] % km^{-1} (Figure 4a). In a cross-section and along the transect of the fan (Appendix I.a), the median sediment accumulation area, without considering any topography, was 20.3 [18.4–22.1] km^2.

The spatial distribution of accommodation space surrounding the central fan (Figure 4b) is constrained by four sections, all recording the same sedimentary unit within an age range of 26.4–24.9 ± 0.25 Ma (Figure S2, Appendix I; Schlunegger, Jordan, et al., 1997; Schlunegger, Leu, et al., 1997; Engesser & Kälin, 2017). The most proximal section (Rigi; Figure S2, Appendix I.b) comprises a 1600 ± 50 m thick suite and was accumulated at a rate of 1070 ± 210 m Myr^{-1}. Farther downstream, 8 km to the East–northeast (Rossberg; Figure S2, Appendix I.b), the same unit thins to 1485 ± 50 m and the accumulation rate decreased to 990 ± 200 m Myr^{-1}. Another 6 km downstream to the East (Sattel; Figure S2, Appendix I.b), the same unit is 1040 ± 50 m thick, and the sediment accumulation rate was 695 ± 150 m Myr^{-1}. The most distant remnants of this unit, situated 7 km farther down-system (Einsiedeln; Figure S2, Appendix I.b), are 595 ± 50 m thick, and the accumulation rate was thus less (400 ± 100 m Myr^{-1}). The calculated median subsidence rate at the apex was 1287 [1041–1549] m Myr^{-1}. It decreased farther downstream at a median rate of 3.97 [2.54–5.59] % km^{-1} (Figure 4b). In a cross-section, the median depositional area (topography excluded) was 23.2 [20.2–26.2] km^2.

In the East, two stratigraphic sections (Toess and Hoernli; Figure S3, Appendix I.c) record the same suite spanning an age between 14.6 and 13.6 ± 0.2 Ma (Kälin & Kempf, 2009; Kempf et al., 1997). At both sites, the sedimentary sequences are 315 m thick and accumulated at an average rate of 240 ± 100 m Myr^{-1} (Figure 4c). Accordingly, this value corresponds to a median subsidence rate (i.e. 240 [118–411] m Myr^{-1}) at the apex. Consequently, the median decreasing rate of the subsidence rate was 0.01 [−8.1–8.2] % km^{-1} (Figure 4c). In a section along distance from proximal to distal, the median depositional area (topography excluded) was 2.9 [1.9–3.8] km^2.

4.2 | Grain size, coefficient of variation and self-similarity variable

On average, the D_{50} is approximately 51 mm for the western fan (73 sites) and 40 mm for both the central (84 sites) and the eastern fans (60 sites) respectively. For the western and central fans, we observe a general trend of decreasing grain sizes down-system, as visible in the field at the scale of individual outcrops (Figure 5). Such downstream fining trends of the D_{50} are not highly pronounced for individual sites along the fans, which show a large scatter in the raw D_{50} values (Figure 6a,b). Yet, these average stratigraphic grain size fining trends become clearer when the data are merged in equally sized bins along distance (Figure 6d,e). For the eastern fan, a grain size fining trend is not clearly visible, neither in the field (Figure 5), neither from the original nor the binned grain size data (Figure 6c,f respectively). When expressed as cumulative distribution curves, the same trends for each fan system are shown, albeit with a large scatter of the data (Figure 7).

For the western fan, the exponential regression fit (Equation 8) of the raw D_{50} yields a median input grain size of $D_A = 103$ [92–116] mm at the system's apex, coupled with a grain size fining rate α of 9.3 [7.9–11] % km^{-1} (Figure 6a). The same regression applied to the binned D_{50} reveals a median $D_A = 87$ [79–105] mm at the system's apex, along with $\alpha = 7.2$ [5.9–9.4] % km^{-1} (Figure 6d). Despite the slightly lower input grain size and grain size fining rate revealed by the regression on the binned data, both

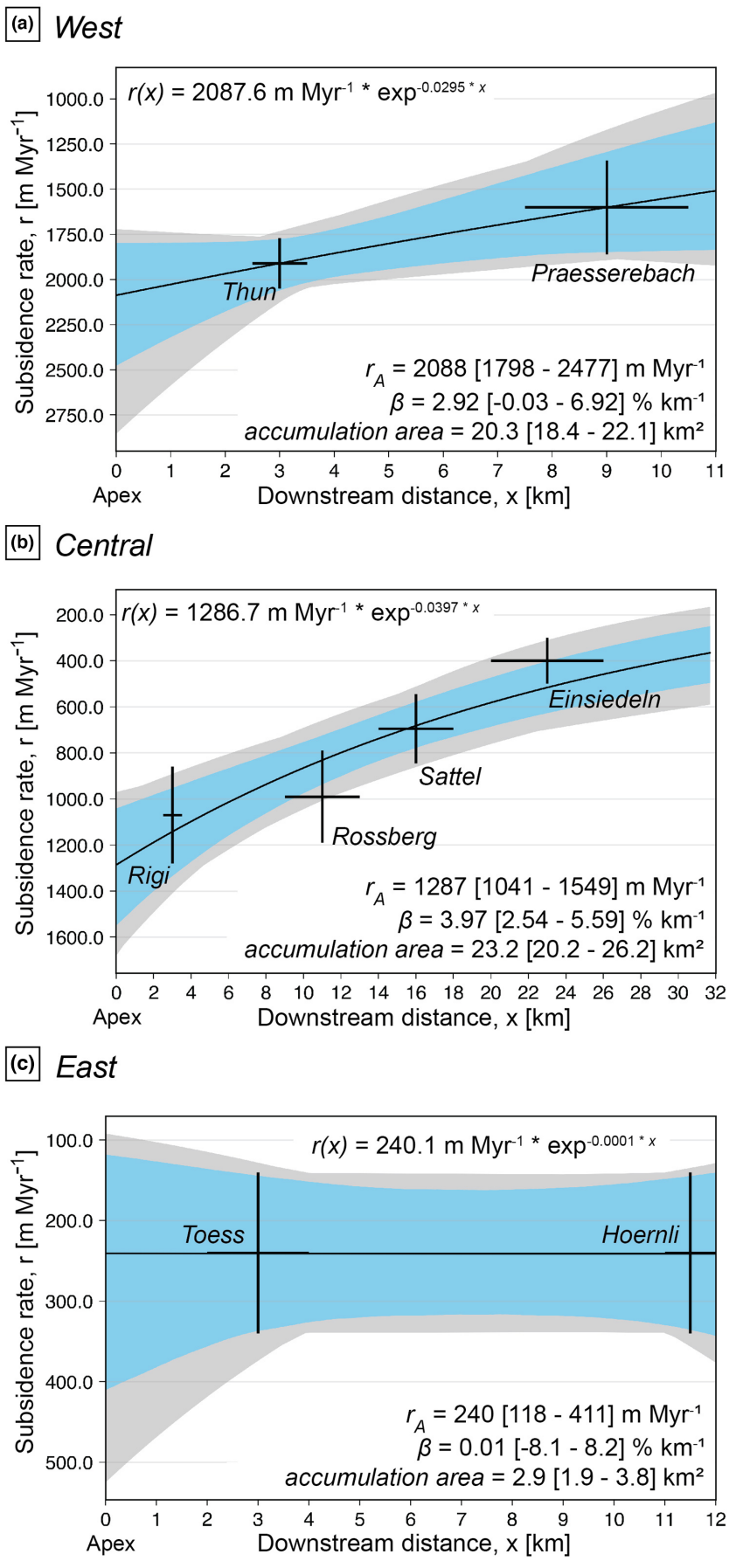

FIGURE 4 Subsidence curves for the base beneath the (a) western, (b) central and (c) eastern fans. The crosses represent stratigraphic sections and uncertainties in their relative position to the apex and the subsidence rates. The black line reflects the best-fit regression curve, the blue area corresponds to the 95% confidence interval (CI) of the exponential regression analyses and the grey area corresponds to all possible regression scenarios thereby using 10^4 iterations. The accumulation area is the cross-sectional area calculated upon using the trapezoidal rule.

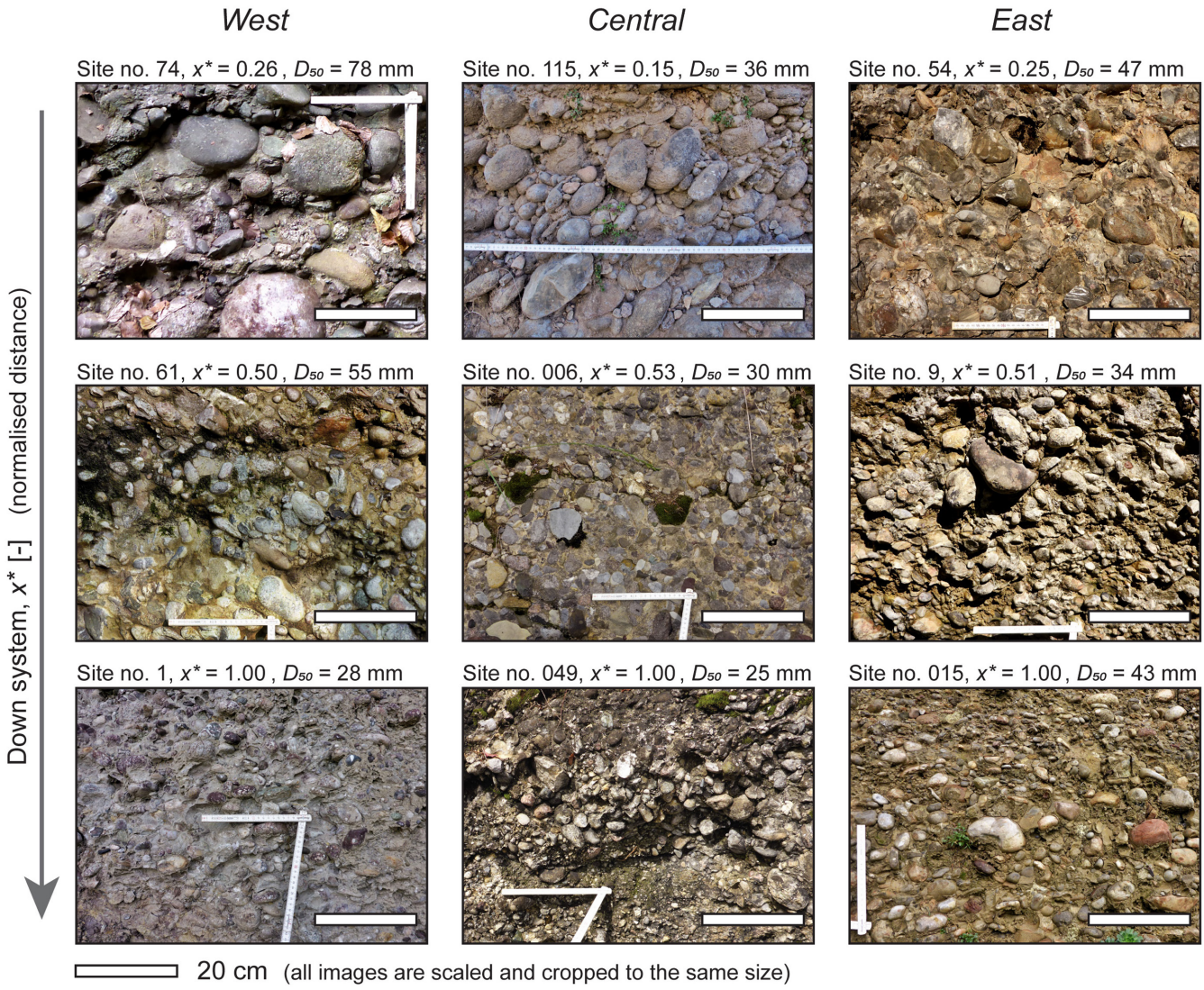

FIGURE 5 Examples of conglomerates and median values of the grain size percentile D_{50} at different sites along the three fans.

datasets demonstrate a clear down-system fining trend (Figure 6a,d respectively) within related uncertainties.

For the central fan, the fit of the raw data results in a median $D_A = 49$ [47–51] mm at the system's apex with $\alpha = 1.4$ [1.1–1.7] % km^{-1} (Figure 6b). The same regression, when applied to the binned data, reveals an almost identical median $D_A = 48$ [46–51] mm at the system's apex, coupled with a slightly higher fining rate $\alpha = 1.5$ [1.1–1.8] % km^{-1} (Figure 6e). While downstream variations in the raw D_{50} values show a significant scatter, making it challenging to identify a clear down-system trend (Figure 6b), the binning of the data reveals a distinct down-system fining trend (Figure 6e).

For the eastern fan, the D_{50} values show a scatter down-system (Figure 6c). The regression fit to the raw data yields a median $D_A = 46$ [43–49] mm at the system's apex, along with a fining rate $\alpha = 2.1$ [1.2–2.9] % km^{-1} (Figure 6c). Binning the data and the application of the same regression thereon result in an almost identical input grain size value of $D_A = 45$ [43–48] mm, coupled with the same fining rate of $\alpha = 2.1$ [1.2–2.9] % km^{-1} (Figure 6f). Yet, the grain size values are slightly larger at distal positions than at intermedial locations along the fan transect (Figure 6c,f), thereby not revealing a clear down-system grain size fining.

The coefficient of variation C_v for the western fan is on average $C_v = 0.67$ [0.57–0.77] and remains mostly stable (Figure 8a). For the central fan, the C_v shows a larger scatter at proximal positions but stabilises farther downstream at an average $C_v = 0.66$ [0.56–0.76] (Figure 8b). The average C_v value for the eastern fan is $C_v = 0.63$ [0.54–0.73] and reveals a slightly decreasing trend towards distal positions (Figure 8c). Despite some scattering of the data at individual sites, the three fans have a very similar average C_v value of 0.65 ± 0.10. This observation suggests a constant ratio between the mean and standard deviation of gravel grain

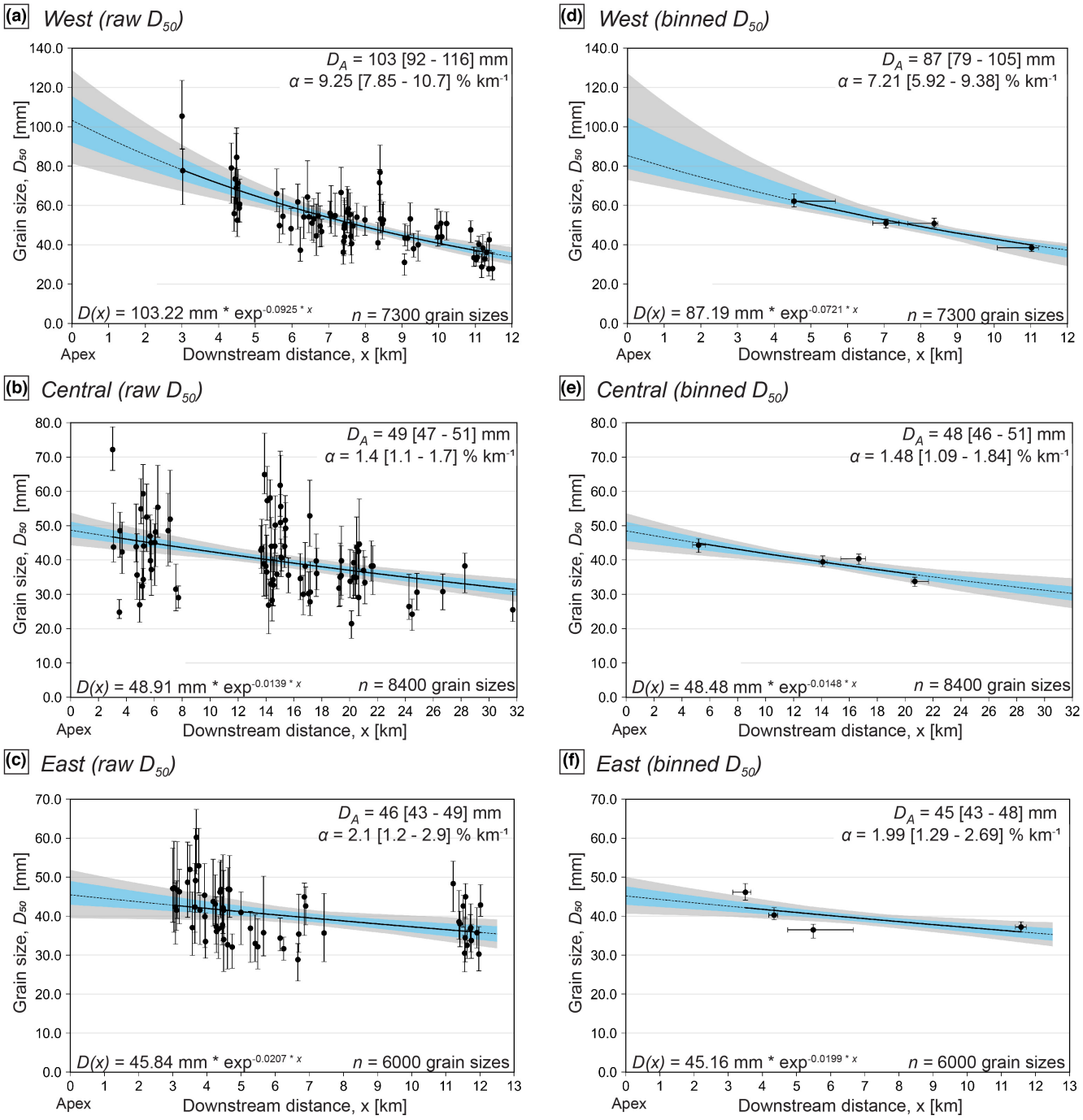

FIGURE 6 Downstream grain size trends of the (a) western, (b) central and (c) eastern fans showing the raw D_{50} data, whereas the binned dataset is shown in (d) for the western, (e) for the central and (f) for the eastern fan. Each bin contains 25% of the data along distance. The black dots correspond to the median values of the D_{50}, the error bars show the 95% confidence interval (CI). The black line reflects the best-fit regression curve (solid = data available; dotted = extrapolated), the blue area corresponds to the 95% CI of the exponential regression analyses and the grey area corresponds to all possible regression scenarios, thereby using 10^4 iterations. The regression curves are extrapolated towards the apex and plus 500 m towards distal positions from the last site.

sizes on these fans. A similar important finding concerns the grain size similarity variable ξ (Equation 5), as illustrated in the cumulative distribution curves (Figure 9a–c). The results indicate that for all sites the grain size distributions (Figure 7) collapse onto self-similar curves (Figure 9a–c) when presented in ξ space. Thus, at a given site the normalised grain size values decrease downsystem at the same rate, reflected by the consistent shape of the similarity variable curves. Although the centres of these (i.e. 50% in Figure 9) are slightly shifted to smaller ξ values, if compared to the curves of a simulated normal distribution (solid black line in Figure 9), the results of

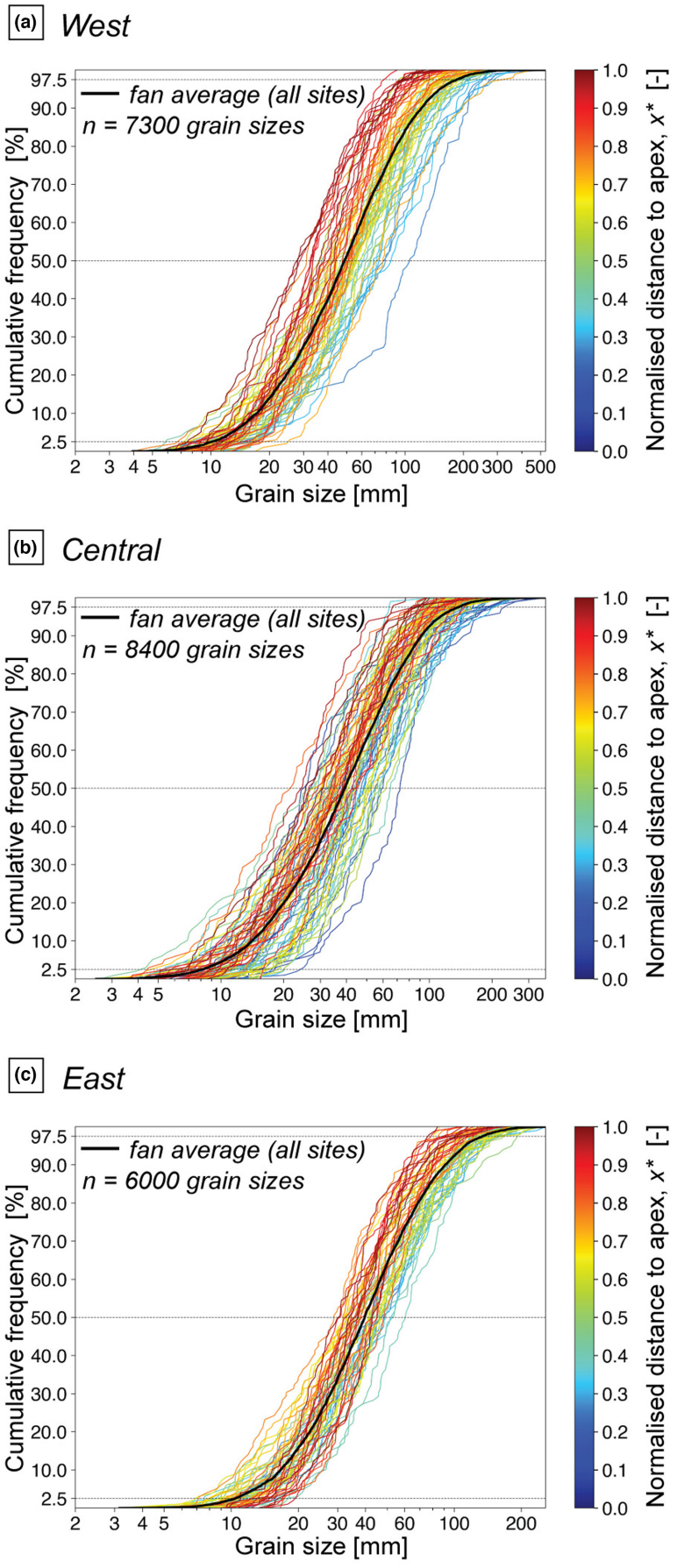

FIGURE 7 Cumulative grain size distributions of the (a) western, (b) central and (c) eastern fans with respect to their relative distance to the apex. The fan average (solid black curve) bases on the data of all individual sites. Note the logarithmic grain size scale.

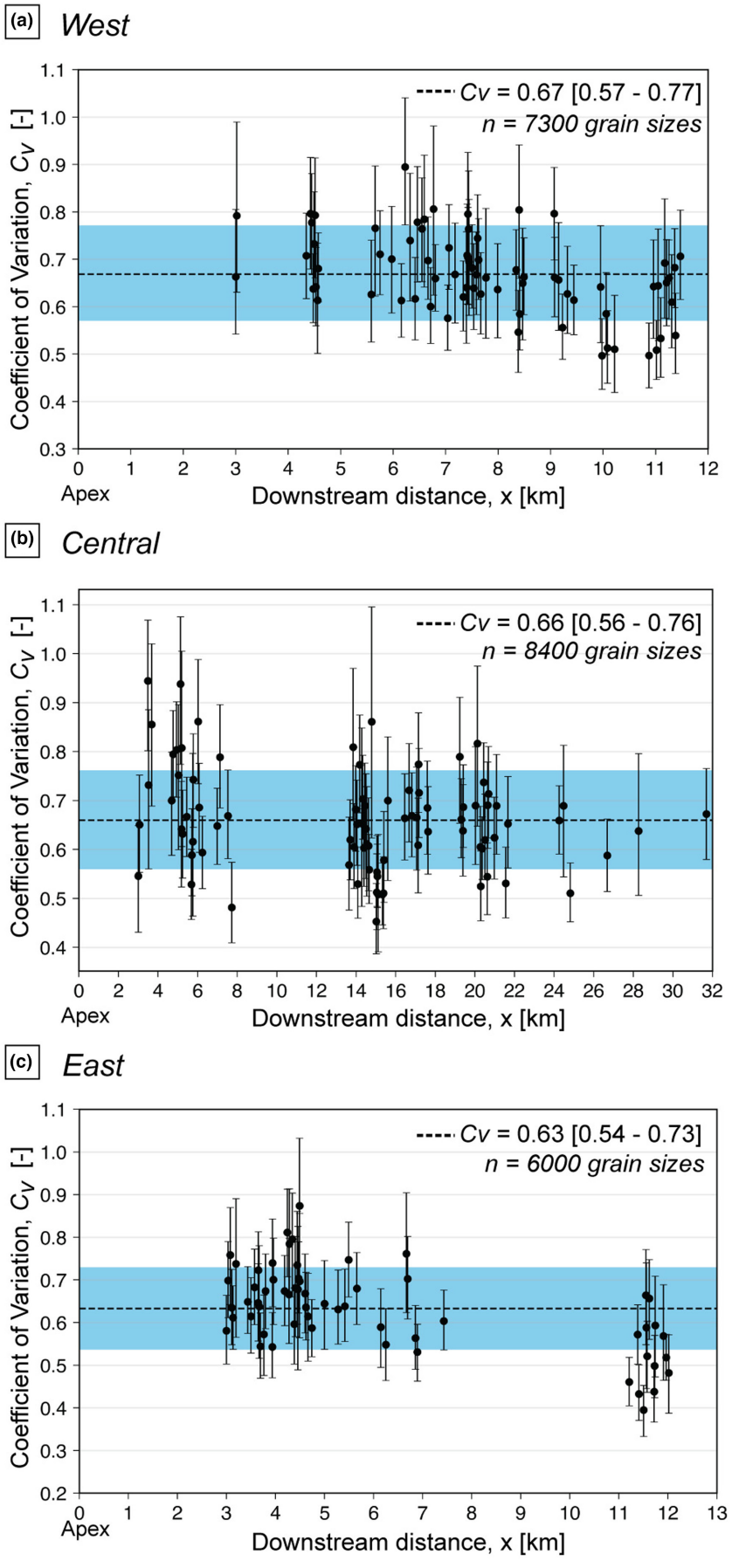

FIGURE 8 Coefficient of variation (C_v) of the (a) western, (b) central and (c) eastern fans along downstream distance. The black dots correspond to the median C_v values, the error bars show the 95% confidence interval (CI). The black dashed horizontal line shows the fan average C_v values and the blue area corresponds to the 95% CI thereof.

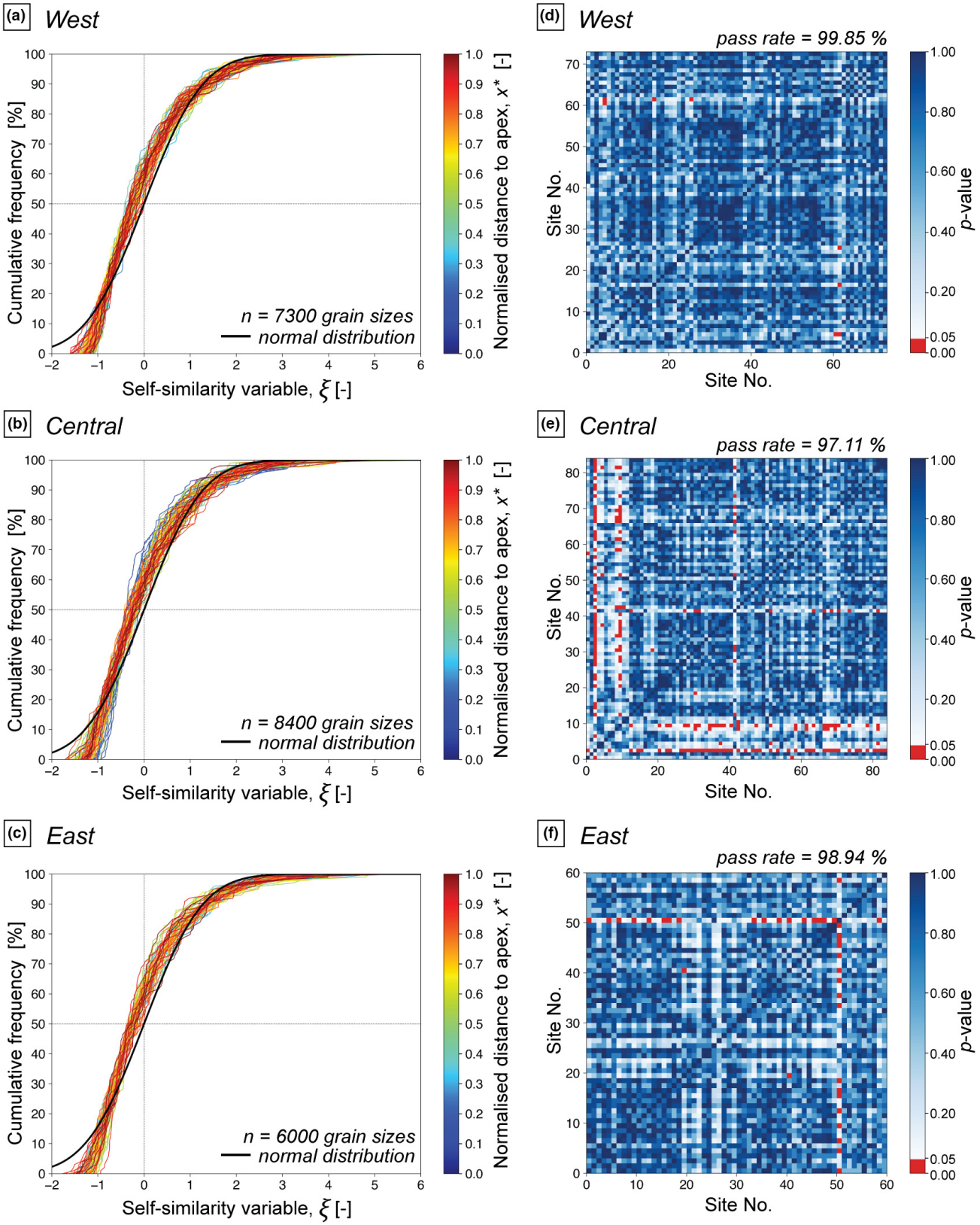

FIGURE 9 Cumulative distributions of the grain size data transformed into the self-similarity variable ξ for the (a) western, (b) central and (c) eastern fans with respect to their relative distance to the apex. The black curves show a simulated normal distribution based on the fan's average ξ value and its standard deviation. Corresponding correlation matrices of the Kolmogorov–Smirnov two-sample test (KS2) for the (d) western, (e) central and (f) eastern fan systems. Blue colours show two ξdistributions that are statistically similar if the reported p value is larger than 0.05 (i.e. alpha level = 95% confidence interval), red colours show distributions that are statistically different to each other.

the KS2 test (Section 3.3.1) confirm that almost all distributions are similar to each other at a significance level of alpha = 0.05 (Figure 9d–f). The site-to-site comparison indicates a success rate of 99.85% of the KS2 test for the western, 97.11% for the central and 98.94% for the eastern fans, confirming the self-similarity of the ξ distributions (Figure 9d–f).

4.3 | Long-term and instantaneous sediment fluxes, and fan intermittencies

The occurrence of self-similar grain size distributions for all three fan systems allows for the application of the self-similar grain size fining model (Fedele & Paola, 2007). Given the high similarity between the outcomes of the exponential fitting regressions on the raw and the binned grain size data, particularly for the central and eastern fans, and the evident down-system fining trend in both datasets for the western fan, we show the model results exclusively applied to the raw datasets (Figure 10). The outcomes of the model, applied to the binned data, are provided in Appendix II.

For the western fan, the model yields a median input sediment flux $Q_{s_A}^*$ of 16.2 [14.3–18.5] km^2 Myr^{-1}, with a median sediment excess rate of F_E = 1.14 [1.05–1.28] (Figure 10a). The model suggests that approximately 88 [78–95] % of the supplied material was deposited on the fan, while 12 [5–22] % was exported out of the system (Figure 10a; median MAE 0.017 [0.012–0.022]). For the central fan, a median $Q_{s_A}^*$ = 40.3 [31.2–51.4] km^2 Myr^{-1} is required to best fit the observed grain size fining rates (median MAE 0.00725 [0.00721–0.00733]), resulting in a median F_E = 2.49 [2.00–3.06]. The model outcomes suggest that approximately 60 [50–67] % of the supplied sediment was exported out of the system, while a median of 40 [33–50] % was deposited on the fan (Figure 10b). In the east, we obtained a median $Q_{s_A}^*$ = 5.7 [3.5–9.9] km^2 Myr^{-1} and a high median sediment excess rate F_E = 2.85 [2.14–4.64], indicating that approximately 65 [53–78] % of the sediment was transferred out of the system, while about 35 [22–47] % of the supplied material accumulated on the fan (Figure 10c; median MAE 0.0045 [0.0044–0.0048]). Alternatively, for the eastern fan, and considering an apex situated +15 km farther upstream of the most proximal site, the model yields a median $Q_{s_A}^*$ = 6.7 [3.2–15.4] km^2 Myr^{-1} and a median sediment excess rate F_E = 1.63 [1.25–2.33], indicating that a median 39 [20–57] % of the sediment was transferred out of the system (see Appendix I.c for figure). Because both results are very similar, we focus on the more conservative solution with an apex placed +3 km farther upstream of the most proximal site for further calculations and discussions.

Calculations of the bedload capacity, or instantaneous bedload fluxes, return median values of approximately: Q_b* = 8870 [3070–24,800] km^2 Myr^{-1} for the western fan, Q_b* = 6150 [2240–16,500] km^2 Myr^{-1} for the central fan and Q_b* = 6370 [2750–14,000] km^2 Myr^{-1} for the eastern fan. Note that the aforementioned values were determined using the data from all sites of each fan. Site-specific bedload fluxes may deviate from these values, as documented by the cumulative distribution curves calculated through bootstrapping for each site (Figure 11). Additionally, these curves reveal a decreasing trend of the bedload fluxes towards distal sites, albeit with some scatter of the data (Figure 11). The large spread of the 95% CI is also reflected by the positive skewness of the bulk data (Figure 11) of each depositional system.

For each fan, the intermittencies are: I_F = 0.0018 [0.00065–0.0053] for the entire western fan, corresponding to an approximate median transport activity of 16 [6–47] h yr^{-1} during which channel-forming bankfull discharge occurred; I_F = 0.0065 [0.0024–0.019] or 57 [21–162] h yr^{-1} for the entire central fan and I_F = 0.00089 [0.00034–0.0024] or 8 [3–21] h yr^{-1} for the entire eastern fan (Figure 12). Alternatively, if the palaeo-fan apex' position of the eastern fan is placed +15 km, the calculations yield I_F = 0.0011 [0.00034–0.0035], corresponding to 9 [3–31] h yr^{-1} (see Appendix I.c for figure). Site-specific intermittency factors show a large spread, especially at the upper tail where the cumulative distribution curves (generated from the bootstrapping data of each site) are right-skewed (Figure 12). For all systems, the intermittency factor increases towards more distal positions (Figure 12), thereby reflecting the opposite trend of the bedload fluxes (Figure 11). All main findings are summarised in Table 1.

5 | INTERPRETATION AND DISCUSSION

The grain size data of the target fans in this study potentially record information on their activities in response to

FIGURE 10 Model outcomes for the (a) western, (b) central and (c) eastern fans for a given input sediment flux $Q_{s_A}^*$. On the left: The grey dots represent the field-derived D_{50} values [raw dataset; error bars correspond to the 95% confidence interval (CI) and the black line reflects the best-fit regression curve on the grain size data (solid = data available; dotted = extrapolated) using Equation (8). The green area corresponds to the 95% CI of the modelled grain sizes D_m (Equations 3 and 6) and the grey area corresponds to all possible scenarios thereby using 10^4 iterations. $Q_{s_A}^*$ = input sediment flux; F_E = sediment excess rate, $Q_{Sexcess}$ = sediment excess in %. On the right: Histograms showing the distribution of the input sediment flux $Q_{s_A}^*$, indicated with the positions of the average, median and 95% CI values.

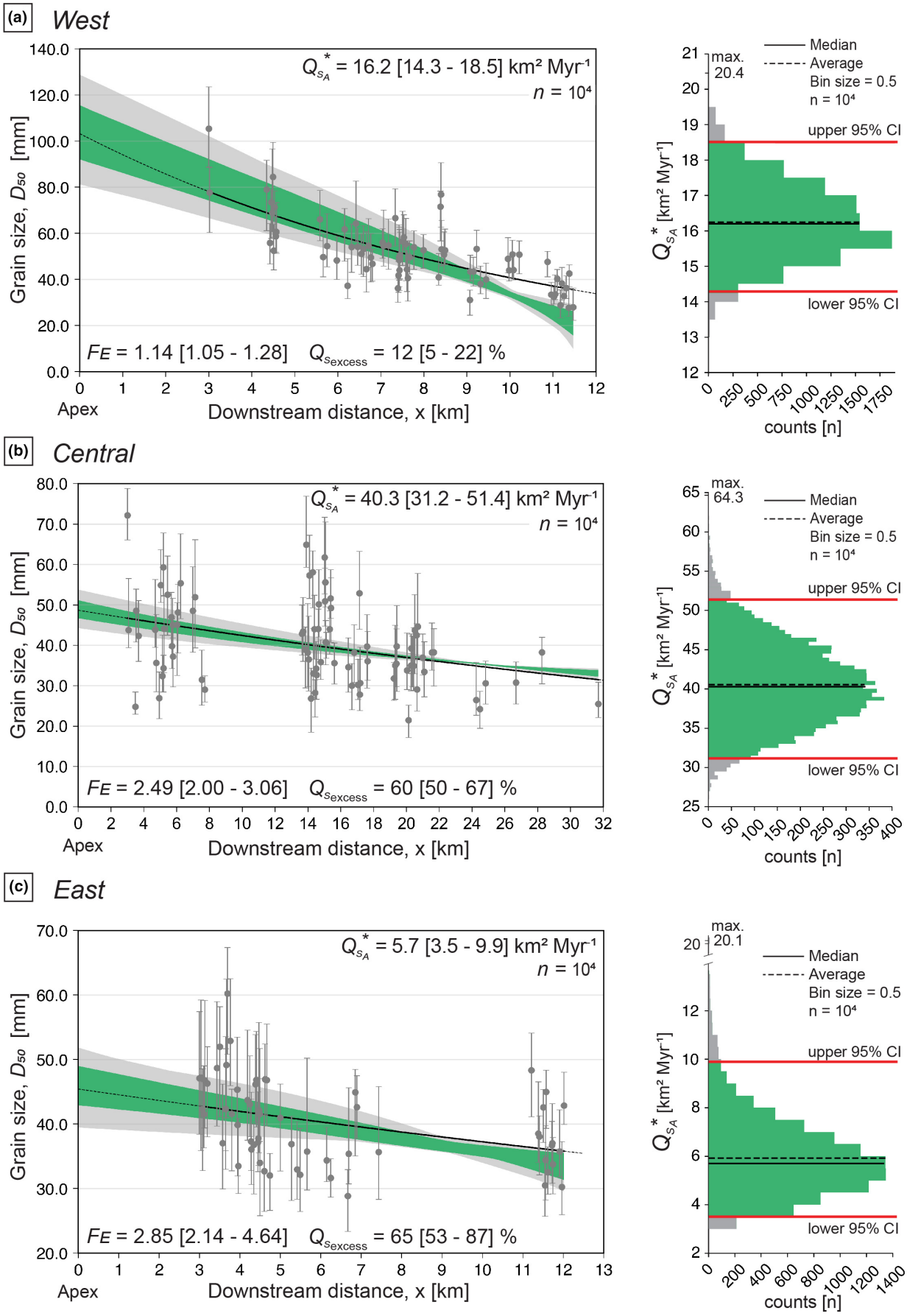

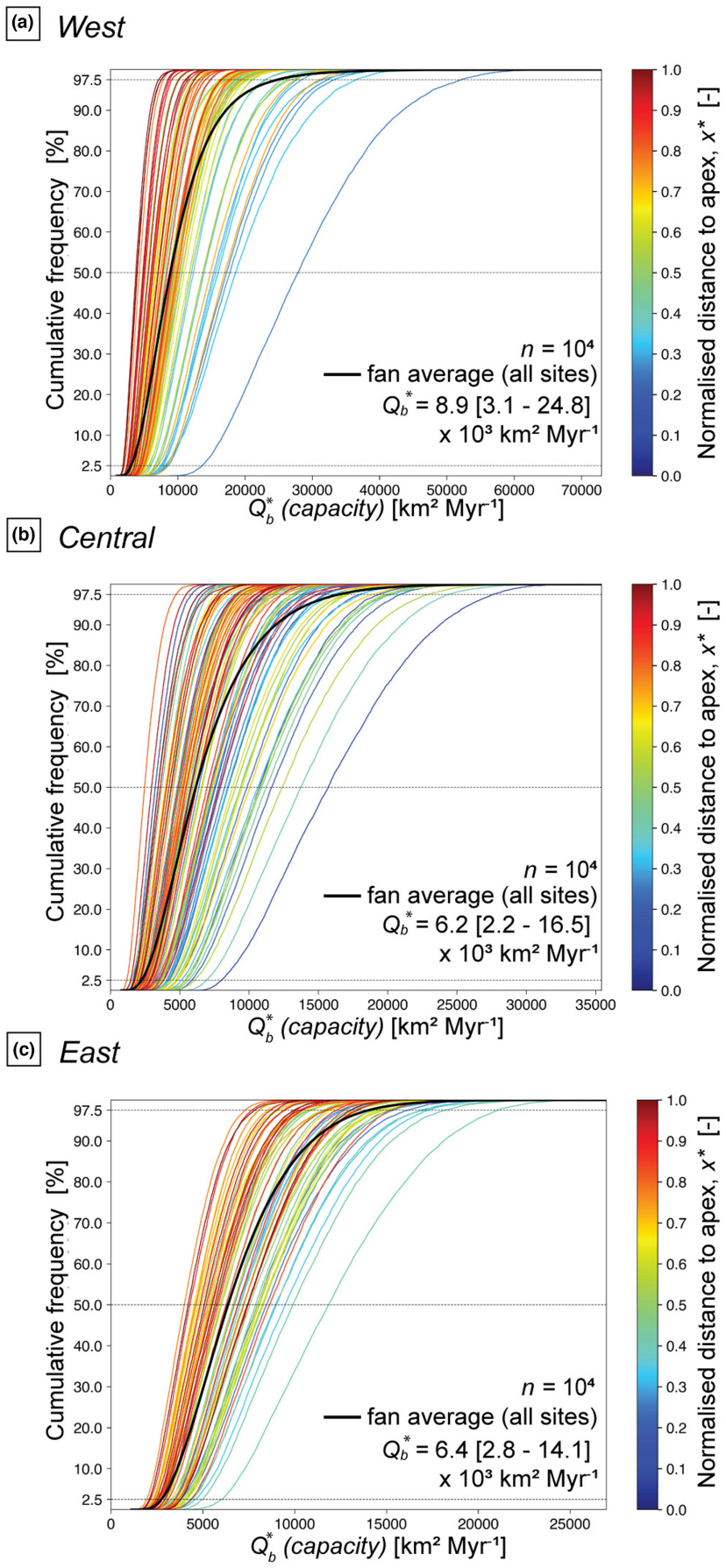

FIGURE 11 Cumulative distributions of the instantaneous bedload sediment flux Q_b* for the (a) western, (b) central and (c) eastern fans with respect to their relative distance to the apex. The individual curves represent the Q_b* values at each analysed site. The black solid line represents the fan average of the bulk data. The numerical values of the median Q_b* along with the 95% confidence interval are indicated for each fan in the lower right of the plots.

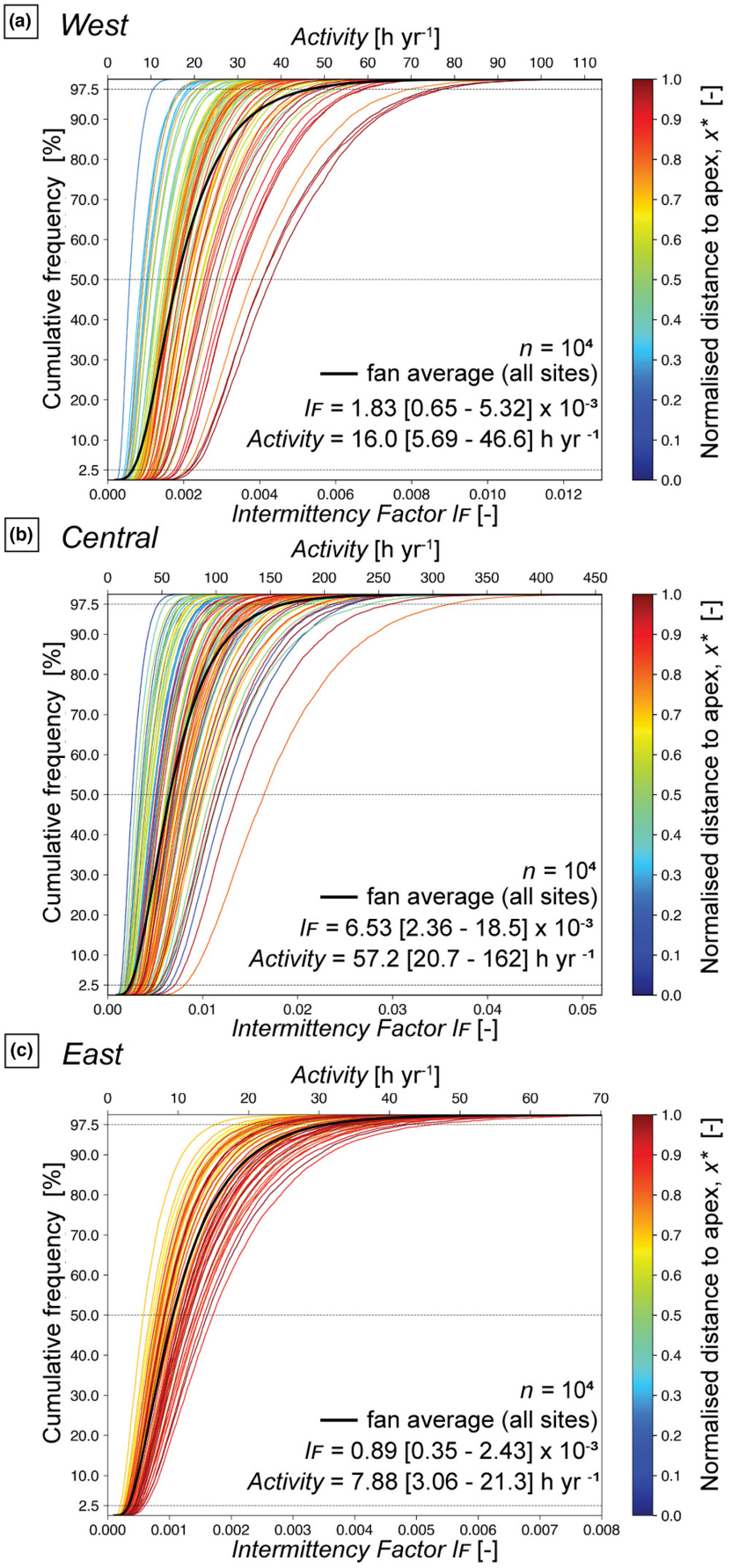

FIGURE 12 Cumulative distributions of the intermittency factors I_F for the (a) western, (b) central and (c) eastern fans with respect to their relative distance to the apex. The I_F is calculated using the ratio between the input sediment flux $Q_{s_A}^*$ and the bedload sediment flux Q_b*. The individual curves show the intermittency factors for each individual site. These values were determined using a bootstrapping approach (see main text and Appendix IV for details). The black solid line represents the fan average of the bulk data. The numerical values of the median I_F and the activity in hours per year, along with the 95% confidence interval, are indicated for each fan in the lower right of the plots.

TABLE 1 Main outcomes of each fan system.

Fan systems	Western	Central	Eastern +3 km	Eastern +15 km
Subsidence rate at apex r_A [m Myr^{-1}]	2088 [1798 to 2477]	1287 [1041 to 1549]	240 [118 to 411]	244 [46 to 1061]
Subsidence change rate β [% km^{-1}]	2.95 [−0.03 to 6.92]	3.97 [2.54 to 5.59]	0.01 [−8.1 to 8.2]	0.01 [−8.1 to 8.2]
Accumulation area [km^2]	20.3 [18.4 to 22.1]	23.2 [20.2 to 26.2]	2.9 [1.9 to 3.8]	5.9 [3.2 to 11.4]
Sediment excess rate F_E [−]	1.14 [1.05 to 1.28]	2.49 [2.00 to 3.06]	2.85 [2.14 to 4.64]	1.63 [1.25 to 2.33]
Grain size at apex D_A [mm]	103 [92 to 116]	49 [47 to 51]	46 [43 to 49]	59 [50 to 70]
Grain size fining rate α [% km^{-1}]	9.25 [7.85 to 10.7]	1.39 [1.10 to 1.69]	2.07 [1.19 to 2.95]	2.07 [1.19 to 2.95]
Long-term sediment flux $Q^*_{S_A}$ [km^2 Myr^{-1}]	16.2 [14.3 to 18.5]	40.3 [31.2 to 51.4]	5.7 [3.5 to 9.9]	6.7 [3.2 to 15.4]
Bedload sediment flux Q_b* [km^2 Myr^{-1}]	8870 [3070 to 24,800]	6150 [2240 to 16,500]	6370 [2750 to 14,000]	6370 [2750 to 14,000]
Intermittency factor I_F [−]	0.001827 [0.00065 to 0.0053]	0.006529 [0.0024 to 0.019]	0.00089 [0.00035 to 0.0024]	0.001056 [0.00034 to 0.0035]
Activity [h yr^{-1}]	16 [6 to 49]	57 [21 to 162]	8 [3 to 21]	9 [3 to 31]

Note: The uncertainties in square brackets correspond to the 95% confidence interval (CI). Find in Appendix I.c the figures for the scenario where the inferred palaeo-apex for the eastern fan was placed at +15 km. Appendix II shows the results and figures related to the model outcomes involving the binned grain size datasets.

either a tectonic control or a climatic driving force, or a combination of both, which we will elaborate in the following through two steps: First, we comment on the sensitivities of our results, we place our results into a context of published work and we discuss how the grain size trends presented in this work can be used to apply the grain size fining model to stratigraphic archives (Section 5.1). Second, we relate the modelling results to possible tectonic and palaeoclimatic interpretations and propose scenarios that led to the fan-formation that is in accordance with our intermittency values (Section 5.2).

5.1 | Grain size trends and intermittencies of Oligo–Miocene alluvial megafans

Our results quantify grain size fining trends for each studied fan, with the western fan showing the most pronounced decreasing trend, while the central and eastern fans revealed a higher scatter of the D_{50} values than the western fan if the raw data are considered (Figure 6a–c). The fining trends become more evident when the stratigraphic data are combined through binning, revealing clear down-system fining in the stratigraphic archives of the western and central fans (Figure 6d,e). However, a clear fining is absent for the eastern fan, as the data largely scatters in the down-system direction, for both, the raw (Figure 6f) and binned D_{50} grain size values. The absence of a clear fining trend might be related to the orientation of the projected proximal–distal trace line (Figure S3a, Appendix I.c), which could be oriented oblique to the actual palaeo-down system direction of the fan. This is likely the case because the palaeo-apex is not preserved anymore and might have been located farther to the Southeast than assumed (Section 2.3). Despite these variabilities in the grain size data, which is consistent with the scatter observed for other (palaeo-) alluvial fan systems (e.g. Brooke et al., 2018; Duller et al., 2010; Whittaker et al., 2011), the standard deviation decreases at the same rate as the mean of the grain size distributions if the data are collapsed into a self-similarity variable ξ (Figure 9a–c). The right skewness of the ξ distributions and the short negative tails are likely explained due to a lack of measurements <2 mm and the occurrence of a few exceptionally large grains (D'Arcy et al., 2017; Harries et al., 2018). Furthermore, the KS2 test results (Section 3.3.1) confirmed that, at almost all sites, the ξ distributions are statistically identical to each other (Figure 9d–f). The coefficients of variation C_v have an average of 0.65 ± 0.10 for all systems (Figure 8), thus falling in the range of values reported in the literature (Armitage et al., 2011; Brooke et al., 2018; Duller et al., 2010; Fedele & Paola, 2007). The ξ and C_v values

derived from the grain size datasets thus indicate that the sorting of a given grain size population is approximately constant and scale invariant at any down-system position. Moreover, the similarity between the ξ values across the three fans suggest that these are decoupled from the source lithology (Appendix I), the climatic and tectonic boundary conditions (Sections 2.2 and 5.2) and probably also the size of the catchments (Schlunegger et al., 1998; Spiegel et al., 2001). Our results suggest that alluvial fan sediments of the SMB have self-similar grain size distributions and sorting properties (Schlunegger et al., 2020). Such characteristics were also documented for the coarse-grained deposits of the Pobla basin adjacent to the Spanish Pyrenees and the Bermejo basin of Argentina (Whittaker et al., 2011 and Harries et al., 2019 respectively), implying similar underlying transport processes on each fan system.

The application of the grain size fining model to our dataset yielded differences in both the annual long-term and instantaneous sediment fluxes for the three depositional systems, resulting in relatively low intermittency factors (Table 1). Among the three fan systems, the central fan stands out as the most active one, displaying the highest intermittency factor. In contrast, both the western and eastern fans had lower intermittency factors, indicating less frequent activity (Table 1). We acknowledge that the spread of the uncertainties on the numerical values is large, which mainly arises from a conservative selection of the model's input parameters and from considering the 95% CI (Table 1). Yet the results align with those of similar studies attempting to estimate sediment fluxes from the stratigraphic record (e.g. Brewer et al., 2020). Thus, our findings provide insights into the activity of Oligo–Miocene alluvial fans, suggesting that the dispersal systems on the fans were capable of transporting the supplied sediment within a few hours to days per year, particularly during relatively short periods when bankfull discharge conditions prevailed. This implies that during periods of low flow, the coarse-grained sediment particles were likely not in transport throughout the rest of the year. This is consistent with interpretations of intermittency values determined for both modern and ancient streams (Hayden et al., 2021; Sharma et al., 2024), thereby highlighting the importance of a few high magnitude discharge events during which effective sediment transport occurs, in both, arid and humid environments (Leenman et al., 2022; Molnar, 2001).

5.2 | Environmental versus tectonic controls

A broader question is whether the long-term sedimentation on these fans was primarily governed by environmental boundary conditions or tectonic processes (Hajek & Straub, 2017; Ventra & Clarke, 2018). Our results show that the western and central fans reveal significant differences in their sediment budgets, and also in their sediment flux intermittencies (Table 1), despite that both systems formed under approximately the same climate (Section 2.2). Hence, if a climate driving force alone would explain the sedimentary dynamics, we would expect similar model outcomes for the central and western fans. Yet, an increase in storminess, as proposed for the study area around ca. 25.5 Ma (Schlunegger & Norton, 2013; Section 2.2) could have enhanced erosion rates in the catchments, thereby increasing sediment supply rates to the basin. From a stratigraphic perspective, climatic signals that are coupled to an increase in the precipitation rates can be recorded as few meters thick sheet conglomerate beds, which are laterally extend over a large area and are embedded within mudstone beds (Armitage et al., 2011; Heller & Paola, 1992). Such morphologies have not been observed in the deposits of the three fans, or maybe have not even been preserved. However, given the timescale during which these fans formed, we acknowledge that short-lived climatic signals can be mitigated or amplified by independent supply signals from other sources (Armitage et al., 2011; Castelltort et al., 2015; Whittaker, 2012), which makes it difficult to identify a climatic driving force in the stratigraphic record. Thus, even if such signals were preserved in our study area, they were likely overpowered by the sedimentary response to a tectonic and orogenic driving force.

As outlined earlier (Section 3.3.4), downstream grain size fining trends can be used to quantify the rates at which sediment was supplied to the basin (Duller et al., 2010; Flemings & Jordan, 1989, 1990; Parsons et al., 2012). For the western fan, a relatively high grain size fining rate was observed, coupled with a relatively high rate at which the subsidence decreased in the downstream direction (Table 1). These high grain size fining rates might suggest a strong tectonic control and could point to an underfilled state of the basin (Section 3.3.4). According to our model, the creation of accommodation space occurred nearly in pace ($F_E = 1.14$) with the volumes of supplied sediment (16.2 km^2 Myr^{-1}). Therefore, any supplied sediment to the western fan is stored within the basin. For the central fan, the situation was different. A large input sediment flux (40.3 km^2 Myr^{-1}) is required to explain the low grain size fining rates in a basin where the subsidence decreased at a high rate downstream (Table 1). This sediment supply outpaced the formation of accommodation space, with the consequence that the basin was largely overfilled ($F_E = 2.49$). As we have ruled out a distinct environmental driven control such as a change in the global or regional climate (see before), we

invoke tectonic controls, particularly in the source area, to explain the differences particularly in the long-term sediment fluxes and thus in the intermittency values. As proposed by Schlunegger and Castelltort (2016) for our study area, the post-collisional slab break-off at ca. 32–30 Ma (Schlunegger & Kissling, 2022), and the subsequent slab roll-back (Kissling & Schlunegger, 2018; Schlunegger & Kissling, 2015) contributed to the surface uplift and increase of the Alpine topography. As a consequence, enhanced surface erosion led to the high sediment fluxes (Kuhlemann, Frisch, Dunkl, & Székely, 2001; Sinclair, 1997) and sediment load concentrations (Garefalakis & Schlunegger, 2018), which caused the rapid propagation of the central fan into the basin. Such a scenario was likely facilitated given the short distance between the central fan and the Lepontine area (Figures 1 and 2), which acted as the major sediment source and experienced a high surface uplift rate in response to the slab break-off at that time (Schlunegger & Castelltort, 2016). Moreover, the high sediment fluxes recorded by the central fan likely promoted the basin to be overfilled, as revealed by the model results (see before), and possibly explain the high sediment transport activities, as implied by the intermittency factor. We note, however, that the erosional signal of slab break-off was recorded in the central fan ca. 3.6–5.6 Ma after the delamination event. This difference in timing was interpreted by Schlunegger and Castelltort (2016) as a delayed secondary response to high surface uplift rates, conditioned by the size of the system and the pattern of exhumed bedrock. For the western fan, the model predicts smaller sediment fluxes and lower activities compared to the central fan (Table 1). The western fan was situated at a larger distance to the Lepontine area (Figure 1) and was formed during a time when the Alps were considered to have reached a balance between crustal uplift and surface erosion, enabling a steady-state elevation from approximately 25–24 Ma onwards following the initial sediment pulse (Schlunegger & Kissling, 2015). We use these mechanisms to explain the decrease in the fan activity after 25 Ma when the western fan was formed and a balance between subsidence and sediment supply was established in the basin (see before).

The eastern fan was formed under a cooler and potentially drier climate than the western and central fans (Section 2.2). As documented for modern Alpine systems, a cooling climate likely yields higher sediment fluxes (Glur et al., 2013), consequently, we would expect relatively large sediment supply rates and high surface dynamics for the eastern fan, which, however, was not the case according to our model (Table 1). Therefore, we consider tectonic controls to be the primary reason for the relatively low supply rates of sediment (5.7 km^2 Myr^{-1}). Our results show that the downstream decrease in subsidence rates was negligible (median of zero; Table 1) and the grain size fining rate was low, but the degree of basin overfill was higher ($F_E = 2.85$) than in the western and central fans. Consequently, we suggest that the observations in the East can be explained by the formation of the Triangle Zone (Section 2.2) that decreased the available accommodation space for sedimentation, promoting the basin to be overfilled. In addition, around 22–20 Ma, the exhumation of the external crystalline massifs and tectonic unroofing in the core of the Alps caused a modification of the drainage network, which could have reduced the sediment supply to the Molasse basin (Schlunegger & Kissling, 2022) and thus lowered the sedimentary dynamics expressed by the low intermittency values of the eastern fan (Table 1). In summary, we suggest that the fan intermittencies elaborated for the three major megafans in the SMB reflect the stratigraphic response to different sediment fluxes driven by the tecto-geomorphic evolution of the Alpine hinterland.

6 | SUMMARY AND CONCLUSIONS

We investigated the sediment routing system's activity, expressed through the intermittency factor, for three Oligo–Miocene palaeo-alluvial megafans, i.e. the western, central and eastern fans, in the SMB. We unravelled this information through calculations of the ratio between the long-term average and short-term instantaneous unit sediment fluxes, thereby analysing the architectural trends and grain sizes preserved in conglomerates. In particular, the rate at which downstream grain size fining occurs depends on the subsidence patterns, which we used to quantify the rates at which sediment was supplied to the SMB, thereby applying a grain size fining model (Fedele & Paola, 2007).

Our stratigraphic grain size analyses indicated a downstream fining trend for all three fans and for both, the raw and the binned D_{50} values, albeit some scatter of the data. Moreover, the three fan systems revealed self-similar grain size properties as expressed by the statistically identical ξ distributions (a normalisation of the grain size data by the mean and the standard deviation), suggesting constant down-system sorting processes. Despite these similarities, all three fans revealed differences in their sediment accumulation rates, which we use as a proxy for the basin's subsidence. These differences are mainly mirrored in the fans' long-term sediment fluxes, but related intermittency factors or the fans' activity are equivalent within uncertainties. Our calculations suggest that the central fan was a more

active system where the supplied sediment (ca. 40.3 km^2 Myr^{-1}) was transported in approximately 57 [21–162] h yr^{-1} (intermittency factor of 0.0065 [0.0024–0.019]) on a yearly basis. The dispersal systems on the western fan revealed a long-term sediment flux of ca. 16.2 km^2 Myr^{-1} and needed 16 [6–49] h yr^{-1} (intermittency factor of 0.0018 [0.00065–0.0053]) to accomplish their transport work on an annual basis, whereas those on the eastern fan transported the supplied sediment (ca. 5.7 km^2 Myr^{-1}) within approximately 8 [3–21] h yr^{-1} (intermittency factor of 0.00089 [0.00035–0.0024]). In summary, the three fans chronicle a temporal change in sediment supply and surface dynamics where the related rates and activities were highest for the central and oldest fan, after which the fluxes decreased through time.

The analysis of our data suggest that tectonics rather than climate likely explained the differences between the studied fans, as these fans evolved during times when major tecto-geomorphic changes occurred in the Central European Alps. We interpret that the formation of the central, more active fan was potentially controlled by the delamination of the European mantle lithosphere argued to have taken place around 32–30 Ma following continent–continent collision (Schlunegger & Kissling, 2022). This resulted in high uplift rates in the area surrounding the Lepontine dome in the Central Alps, which was the major source area of the systems feeding the central fan. In contrast, the western fan, forming a few million years later, did not record the signal of enhanced surface erosion, as expressed by the lower long-term sediment fluxes. In the East, during the Middle Miocene, the third and probably least active system evolved when the Triangle Zone in the SMB was formed and the drainage network in the Alps underwent a reorganisation, which is reflected in the low sediment supply rate.

In summary, we provided estimates on the activity of these Oligo–Miocene megafans, stating that the dispersal systems could accomplish their annual sediment transport work within a couple of hours or a few days, thereby reflecting the occurrence of a few high-magnitude discharge events on a yearly basis. Accordingly, we show that reconstructions of the sediment flux budgets and intermittencies for these alluvial megafans provide insights not only into the evolution of the adjacent mountain belts, but also offer a valuable tool to understand the dynamics of these sedimentary routing systems in the geological past. When applied to Oligo–Miocene conglomerates of the Swiss Molasse foreland basin, such data allow us to unravel the tecto-geomorphic development of the evolving Central Alps across temporal scales.

ACKNOWLEDGEMENTS

The authors would like to thank Wonsuck Kim for the editorial handling and helpful review of this work. Additionally, we would like to thank John Armitage for the insightful and constructive review, which helped to strengthen the arguments made in this work and to clarify our thoughts. We acknowledge open access funding by the University of Bern, Switzerland. Open access funding provided by Universitat Bern.

FUNDING INFORMATION

PG received funding from the Swiss National Science Foundation (SNFS), Grant No. P1BEP2_200189.

CONFLICT OF INTEREST STATEMENT

The authors declare that they do not have any competing interests.

DATA AVAILABILITY STATEMENT

Field and additional data are available in the article supporting information.

ORCID

Philippos Garefalakis https://orcid.org/0000-0002-6171-1258
David Mair https://orcid.org/0000-0002-7018-6416

REFERENCES

Allen, P. A., Armitage, J. J., Carter, A., Duller, R. A., Michael, N. A., Sinclair, H. D., Whitchurch, A. L., & Whittaker, A. C. (2013). The *Qs* problem: Sediment volumetric balance of proximal foreland basin systems. *Sedimentology*, *60*, 102–130. https://doi.org/10.1111/sed.12015

Allen, P. A., Crampton, S. L., & Sinclair, H. D. (1991). The inception and early evolution of the north Alpine foreland basin, Switzerland. *Basin Research*, *3*, 143–163. https://doi.org/10.1111/j.1365-2117.1991.tb00124.x

Anfinson, O. A., Stockli, D. F., Miller, J. C., Möller, A., & Schlunegger, F. (2020). Tectonic exhumation of the central Alps recorded by detrital zircon in the Molasse Basin, Switzerland. *Solid Earth*, *11*, 2197–2220. https://doi.org/10.5194/se-11-2197-2020

Armitage, J. J., Allen, P. A., Burgess, P. M., Hampson, G. J., Whittaker, A. C., Duller, R. A., & Michael, N. A. (2015). Sediment transport model for the Eocene Escanilla sediment-routing system: Implications for the uniqueness of sequence stratigraphic architectures. *Journal of Sedimentary Research*, *85*(12), 1510–1524. https://doi.org/10.2110/jsr.2015.97

Armitage, J. J., Duller, R. A., Whittaker, A. C., & Allen, P. A. (2011). Transformation of tectonic and climatic signals from source to sedimentary archive. *Nature Geoscience*, *4*, 231–235. https://doi.org/10.1038/ngeo1087

Büchi, U. P. (1958). Zur Geologie der Oberen Süsswassermolasse (OSM) zwischen Töss- und Glattal. *Eclogae Geologicae Helvetiae*, *51*, 73–105 (in German). https://doi.org/10.5169/seals-162429

Bürgisser, H. M. (1980). *Zur Mittel-Miozänen Sedimentation im nordalpinen Molassebecken: Das "Appenzellergranit"-Leitniveau des Hörnli-Schuttfächers (OSM)* (PhD thesis, 196 p). ETH Zurich (in German). https://doi.org/10.3929/ethz-a-000218245

Bürgisser, H. M. (1981). Fazies und Paläohydrogeologie der Oberen Süsswassermolasse im Hörnli-Fächer (Nordostschweiz). *Eclogae Geologicae Helvetiae*, *1*, 19–28. (in German). https://doi.org/10.5169/seals-165087

Baran, R., Friedrich, A. M., & Schlunegger, F. (2014). The late Miocene to Holocene erosion pattern of the Alpine foreland basin reflects Eurasian slab unloading beneath the western Alps rather than global climate change. *Lithosphere*, *6*, 124–131. https://doi.org/10.1130/L307.1

Beaumont, C. (1981). Foreland Basins. *Geophysical Journal International*, *65*, 291–329. https://doi.org/10.1002/9781444303810

Beaumont, C., Ellis, S., Hamilton, J., & Fullsack, P. (1996). Mechanical model for the tectonics of doubly vergent compressional orogens. *Geology*, *24*, 675–678. https://doi.org/10.1130/0091-7613(1993)021<0371:MMFTTO>2.3.CO;2

Benavides, S. J., Deal, E., Rushlow, M., Venditti, J. G., Zhang, Q., Kamrin, K., & Perron, J. T. (2022). The impact of intermittency on bed load sediment transport. *Geophysical Research Letters*, *49*, 1–18. https://doi.org/10.1029/2021GL096088

Berger, J.-P. (1992). Paléontologie de la Molasse de Suisse occidentale: Taxinomie, Biostratigraphie, Paléoecologie, Paléogéographie, Paléoclimatologie. Habilitation thesis, 405 pp (in French).

Bernard, T., Sinclair, H. D., Gailleton, B., & Fox, M. (2021). Formation of longitudinal river valleys and the fixing of drainage divides in response to exhumation of crystalline basement. *Geophysical Research Letters*, *48*, 1–9. https://doi.org/10.1029/2020GL092210

Blair, T. C., & McPherson, J. G. (1994). Alluvial fan processes and forms. In A. J. Parsons & A. D. Abrahams (Eds.), *Geomorphology of desert environments* (pp. 354–402). Chapman & Hall. https://doi.org/10.1007/978-94-015-8254-4_14.

Blom, A., Viparelli, E., & Chavarrías, V. (2016). The graded alluvial river: Profile concavity and downstream fining. *Geophysical Research Letters*, *43*, 6285–6293. https://doi.org/10.1002/2016GL068898

Bolliger, T. (1998). Age and geographic distribution of the youngest Upper Freshwater Molasse (OSM) of eastern Switzerland. *Eclogae Geologicae Helvetiae*, *91*, 321–332. https://doi.org/10.5169/seals-168426

Boothroyd, J. C., & Ashley, G. M. (1975). Processes, bar morphology, and sedimentary structures on braided outwash fans, northeastern Gulf of Alaska. *Glaciofluvial Glaciolacustrine Sediment*, *23*, 193–222. https://doi.org/10.2110/pec.75.23.0193

Boston, K. R., Rubatto, D., Hermann, J., Engi, M., & Amelin, Y. (2017). Geochronology of accessory allanite and monazite in the Barrovian metamorphic sequence of the Central Alps, Switzerland. *Lithos*, *286–287*, 502–518. https://doi.org/10.1016/j.lithos.2017.06.025

Brewer, C. J., Hampson, G. J., Whittaker, A. C., Roberts, G. G., & Watkins, S. E. (2020). Comparison of methods to estimate sediment flux in ancient sediment routing systems. *Earth Science Reviews*, *207*, 1–16. https://doi.org/10.1016/j.earscirev.2020.103217

Bridge, J. (1985). Paleochannel patterns inferred from alluvial deposits: A critical evaluation. *Journal of Sedimentary Petrology*, *55*, 579–589. https://doi.org/10.1017/CBO9781107415324.004

Brooke, S. A. S., Whittaker, A. C., Armitage, J. J., D'Arcy, M., & Watkins, S. E. (2018). Quantifying sediment transport dynamics on alluvial fans from spatial and temporal changes in grain size, Death Valley, California. *Journal of Geophysical Research - Earth Surface*, *123*, 2039–2067. https://doi.org/10.1029/2018JF004622

Cande, S. C., & Kent, D. V. (1995). Revised calibration of the geomagnetic polarity timescale for the late Cretaceous and Cenozoic. *Journal of Geophysical Research*, *100*, 6093–6095.

Castelltort, S., Whittaker, A. C., & Vergés, J. (2015). Tectonics, sedimentation and surface processes: From the erosional engine to basin deposition, *1846*, 1839–1846. https://doi.org/10.1002/esp.3769

Cederbom, C. E., van der Beek, P. A., Schlunegger, F., Sinclair, H. D., & Oncken, O. (2011). Rapid extensive erosion of the North Alpine foreland basin at 5–4 Ma. *Basin Research*, *23*, 528–550. https://doi.org/10.1111/j.1365-2117.2011.00501.x

Church, M. (2006). Bed material transport and the morphology of Alluvial River channels. *Annual Review of Earth and Planetary Sciences*, *34*, 325–354. https://doi.org/10.1146/annurev.earth.33.092203.122721

D'Arcy, M., Whittaker, A. C., & Roda-Boluda, D. C. (2017). Measuring alluvial fan sensitivity to past climate changes using a self-similarity approach to grain-size fining, Death Valley, California. *Sedimentology*, *64*, 388–424. https://doi.org/10.1111/sed.12308

Duller, R. A., Whittaker, A. C., Fedele, J. J., Whitchurch, A. L., Springett, J., Smithells, R., Fordyce, S., & Allen, P. A. (2010). From grain size to tectonics. *Journal of Geophysical Research - Earth Surface*, *115*, 1–19. https://doi.org/10.1029/2009JF001495

Dury, G. H. (1961). Bankfull discharge: An example of its statistical relationships. *Hydrological Sciences Journal*, *6*, 48–55. https://doi.org/10.1080/02626666109493230

Engesser, B., & Kälin, D. (2017). Eomys Helveticus N. Sp. and Eomys Schluneggeri N. Sp., two new small Eomyids of the Chattian (MP25/MP26) subalpine lower freshwater Molasse of Switzerland. *Fossil Imprint*, *73*, 213–224. https://doi.org/10.1515/if-2017-0012

Eynatten, H. V. (2003). Petrography and chemistry of sandstones from the Swiss Molasse Basin: An archive of the Oligocene to Miocene evolution of the Central Alps. *Sedimentology*, *50*, 703–724. https://doi.org/10.1046/j.1365-3091.2003.00571.x

Fedele, J. J., & Paola, C. (2007). Similarity solutions for fluvial sediment fining by selective deposition. *Journal of Geophysical Research - Earth Surface*, *112*, 1–13. https://doi.org/10.1029/2005JF000409

Ferguson, R., Hoey, T., Wathen, S., & Werritty, A. (1996). Field evidence for rapid downstream fining of river gravels through selective transport. *Geology*, *24*, 179–182. https://doi.org/10.1130/00917613(1996)024<0179:FEFRDF>2.3.CO;2

Flemings, P. B., & Jordan, T. E. (1989). A synthetic stratigraphic model of foreland basin development. *Journal of Geophysical Research - Solid Earth*, *94*, 3851–3866. https://doi.org/10.1029/JB094iB04p03851

Flemings, P. B., & Jordan, T. E. (1990). Stratigraphic modeling of foreland basins: Interpreting thrust deformation and lithosphere rheology. *Geology*, *18*, 430–434. https://doi.org/10.1130/0091-7613(1990)018<0430:SMOFBI>2.3.CO;2

Garefalakis, P., do Prado, A. H., Mair, D., Douillet, G. A., Nyffenegger, F., & Schlunegger, F. (2023). Comparison of three grain size measuring methods applied to coarse-grained gravel deposits. *Sedimentary Geology*, *446*, 106340. https://doi.org/10.1016/j.sedgeo.2023.106340

Garefalakis, P., & Schlunegger, F. (2018). Link between concentrations of sediment flux and deep crustal processes beneath the European Alps. *Scientific Reports*, *8*, 183. https://doi.org/10.1038/s41598-017-17182-8

Glur, L., Wirth, S. B., Büntgen, U., Gilli, A., Haug, G. H., Schär, C., Beer, J., & Anselmetti, F. S. (2013). Frequent floods in the European Alps coincide with cooler periods of the past 2500 years. *Scientific Reports*, *3*, 1–5. https://doi.org/10.1038/srep02770

Gradstein, F. M., Ogg, J. G., Schmitz, M. D., & Ogg, G. M. (2020). *Geologic time scale 2020* (1st ed., p. 1390). Elsevier. ISBN: 9780128243602.

Hajek, E. A., & Straub, K. M. (2017). Autogenic sedimentation in clastic stratigraphy. *Annual Review of Earth and Planetary Sciences*, *45*, 681–709. https://doi.org/10.1146/annurev-earth-063016-015935

Hantke, R., Letsch, D., Felber, P., Baumeler, A., Heinz, R., Uttinger, J., & Grünig, A. (2022). *Blatt 1152 Ibergeregg.—Geol. Atlas Schweiz 1:25000, Erläut*. 175. (in German) www.swisstopo.ch

Harries, R. M., Kirstein, L. A., Whittaker, A. C., Attal, M., & Main, I. (2019). Impact of recycling and lateral sediment input on grain size fining trends—Implications for reconstructing tectonic and climate forcings in ancient sedimentary systems. *Basin Research*, *31*, 866–891. https://doi.org/10.1111/bre.12349

Harries, R. M., Kirstein, L. A., Whittaker, A. C., Attal, M., Peralta, S., & Brooke, S. (2018). Evidence for self-similar Bedload transport on Andean alluvial fans, Iglesia Basin, South Central Argentina. *Journal of Geophysical Research—Earth Surface*, *123*, 2292–2315. https://doi.org/10.1029/2017JF004501

Harvey, A. M., Mather, A. E., & Stokes, M. (2005). *Alluvial fans: Geomorphology, sedimentology, dynamics* (1st ed., p. 256). Geological Society of London. ISBN: 1862391890.

Hay, W. W., Wold, C. N., & Herzog, J. M. (1992). Preliminary mass-balance 3D reconstructions of the Alps and the surrounding areas during the Miocene. In R. Pflug & J. W. Harbaugh (Eds.), *Computer graphics in geology*. Lecture Notes in Earth Sciences (Vol. *41*, pp. 99–110). Springer. https://doi.org/10.1007/BFb0117790

Hayden, A. T., Lamb, M. P., & McElroy, B. J. (2021). Constraining the timespan of fluvial activity from the intermittency of sediment transport on earth and Mars. *Geophysical Research Letters*, *48*, 1–13. https://doi.org/10.1029/2021GL092598

Heller, P. L., & Paola, C. (1992). The large-scale dynamics of grain-size variation in alluvial basins, 2: Application to syntectonic conglomerate. *Basin Research*, *4*, 91–102. https://doi.org/10.1111/j.1365-2117.1992.tb00146.x

Herwegh, M., Berger, A., Baumberger, R., Wehrens, P., & Kissling, E. (2017). Large-scale crustal-block-extrusion during Late Alpine collision. *Scientific Reports*, *7*, 1–10. https://doi.org/10.1038/s41598-017-00440-0

Hodges, J. L. (1958). The significance probability of the Smirnov two-sample test. *Arkiv för matematik*, *3*, 469–486. https://doi.org/10.1007/BF02589501

Hoey, T. B., & Bluck, B. J. (1999). Identifying the controls over downstream fining of river gravels. *Journal of Sedimentary Research*, *69*, 40–50. https://doi.org/10.2110/jsr.69.40

Huggenberger, P., & Regli, C. (2009). *A Sedimentological model to characterize Braided River deposits for hydrogeological applications* (pp. 51–74). Braided Rivers. https://doi.org/10.1002/9781444304374.ch3

Jordan, T. E. (1981). Thrust loads and foreland basin evolution, cretaceous, Western United States. *American Association of Petroleum Geologists Bulletin*, *65*, 2506–2520. https://doi.org/10.1306/03b599f4-16d1-11d7-8645000102c1865d

Julien, P. Y. (2010). *Erosion and sedimentation*. Cambridge University Press 2. https://doi.org/10.1017/CBO9780511806049

Kälin, D., & Kempf, O. (2009). High-resolution stratigraphy from the continental record of the Middle Miocene Northern Alpine Foreland Basin of Switzerland. *Neues Jahrbuch für Geol. Und Paläontologie—Abhandlungen*, *254*, 177–235. https://doi.org/10.1127/0077-7749/2009/0010

Kästle, E. D., Rosenberg, C., Boschi, L., Bellahsen, N., Meier, T., & El-Sharkawy, A. (2020). Slab break-offs in the Alpine subduction zone. *International Journal of Earth Sciences*, *109*, 587–603. https://doi.org/10.1007/s00531-020-01821-z

Kühni, A., & Pfiffner, O. A. (2001). Drainage patterns and tectonic forcing: A model study for the Swiss Alps. *Basin Research*, *13*, 169–197. https://doi.org/10.1046/j.1365-2117.2001.00146.x

Kempf, O., Bolliger, T., Kälin, D., Engesser, B., & Matter, A. (1997). New magnetostratigraphic calibration of early to middle Miocene mammal biozones of the North Alpine Foreland Basin. In J. Aguilar, S. Legendre, & J. Michaux (Eds.), *Actes du Congrès BiochroM'97* (pp. 547–561). Ecole Pratique des Hautes Etudes, Institut de Montpellier.

Kempf, O., & Matter, A. (1999). Magnetostratigraphy and depositional history of the upper freshwater Molasse (OSM) of eastern Switzerland. *Eclogae Geologicae Helvetiae*, *92*, 97–103. https://doi.org/10.5169/seals-168650

Kempf, O., Matter, A., Burbank, D. W., & Mange, M. (1999). Depositional and structural evolution of a foreland basin margin in a magnetostratigraphic framework: The eastern Swiss Molasse Basin. *International Journal of Earth Sciences*, *88*, 253–275. https://doi.org/10.1007/s005310050263

Kempf, O., & Pfiffner, O. A. (2004). Early Tertiary evolution of the North Alpine Foreland Basin of the Swiss Alps and adjoining areas. *Basin Research*, *16*, 549–567. https://doi.org/10.1111/j.1365-2117.2004.00246.x

Kissling, E., & Schlunegger, F. (2018). Rollback orogeny model for the evolution of the Swiss Alps. *Tectonics*, *37*, 1097–1115. https://doi.org/10.1002/2017TC004762

Krsnik, E., Methner, K., Campani, M., Botsyun, S., Mutz, S. G., Ehlers, T. A., Kempf, O., Fiebig, J., Schlunegger, F., & Mulch, A. (2021). Miocene high elevation in the Central Alps. *Solid Earth*, *12*, 2615–2631. https://doi.org/10.5194/se-12-2615-2021

Kuhlemann, J. (2000). Post-collisional sediment budget of Circum-Alpine Basins (Central Europe). *Memorie degli Studi di Geologia e Mineralogia del Universita di Padova*, *52*, 1–93.

Kuhlemann, J. (2007). Paleogeographic and paleotopographic evolution of the Swiss and Eastern Alps since the Oligocene. *Global and Planetary Change*, *58*, 224–236. https://doi.org/10.1016/j.gloplacha.2007.03.007

Kuhlemann, J., Frisch, W., Dunkl, I., & Székely, B. (2001). Quantifying tectonic versus erosive denudation by the sediment budget: The Miocene core complexes of the Alps. *Tectonophysics*, *330*, 1–23. https://doi.org/10.1016/S0040-1951(00)00209-2

Kuhlemann, J., Frisch, W., Dunkl, I., Szekely, B., & Spiegel, C. (2001). Miocene shifts of the drainage divide in the Alps and their foreland basin. *Zeitschrift für Geomorphologie*, *45*, 239–265. https://doi.org/10.1127/zfg/45/2001/239

Kuhlemann, J., & Kempf, O. (2002). Post-Eocene evolution of the North Alpine Foreland Basin and its response to Alpine tectonics. *Sedimentary Geology*, *152*, 45–78. https://doi.org/10.1016/S0037-0738(01)00285-8

Leenman, A. S., Eaton, B. C., & MacKenzie, L. G. (2022). Floods on alluvial fans: Implications for reworking rates, morphology and fan hazards. *Journal of Geophysical Research – Earth Surface*, *127*, 1–17. https://doi.org/10.1029/2021JF006367

Litty, C., Schlunegger, F., & Viveen, W. (2017). Possible threshold controls on sediment grain properties of Peruvian coastal river basins. *Earth Surface Dynamics*, *5*, 571–583. https://doi.org/10.5194/esurf-5-571-2017

Lourens, L. J., Hilgen, F. J., Laskar, J., Shackleton, N. J., & Wilson, D. (2004). The Neogene period. In F. M. Gradstein, J. G. Ogg, & A. G. Smith (Eds.), *A Geologic Time Scale 2004* (pp. 409–440). Cambridge University Press.

Lyster, S. J., Whittaker, A. C., Farnsworth, A., & Hampson, G. J. (2022). Constraining flow and sediment transport intermittency in the geological past. *Geological Society of America Bulletin*. https://doi.org/10.1130/B36873.1

Mair, D., do Prado, A. H., Garefalakis, P., Lechmann, A., & Schlunegger, F. (2022). Grain size of fluvial gravel bars from close-range UAV imagery – Uncertainty in segmentation-based data. *Earth Surface Dynamics*, *10*, 953–973. https://doi.org/10.5194/esurf-10-953-2022

Matter, A. (1964). Sedimentologische Untersuchungen im östlichen Napfgebiet (Entlebuch—Tal der Grossen Fontanne, Kt. Luzern). *Eclogae Geologicae Helvetiae*, *57*, 315–429 (in German).

Matter, A., Homewood, P., Caron, C., Rigassi, D., van Stuijvenberg, J., Weidmann, M., & Winkler, W. (1980). Flysch and Molasse of western and central Switzerland. In P. Homewood & R. Trümpy (Eds.), *Geology of Switzerland: A guide book. Part B geological excursions* (pp. 261–293). Wepf & Co.

Matter, A., & Weidmann, M. (1992). Tertiary sedimentation in the Swiss Molasse: An overview. *Eclogae Geologicae Helvetiae*, *85*, 776–777. https://doi.org/10.5169/seals-167041

Mazurek, M., Hurford, A. J., & Leu, W. (2006). Unravelling the multistage burial history of the Swiss Molasse Basin: Integration of apatite fission track, vitrinite reflectance and biomarker isomerisation analysis. *Basin Research*, *18*, 27–50. https://doi.org/10.1111/j.1365-2117.2006.00286.x

McLeod, J. S., Wood, J., Lyster, S. J., Valenza, J. M., Spencer, A. R. T., & Whittaker, A. C. (2023). Quantitative constraints on flood variability in the rock record. *Nature Communications*, *14*, 1–12. https://doi.org/10.1038/s41467-023-38967-8

Methner, K., Campani, M., Fiebig, J., Löffler, N., Kempf, O., & Mulch, A. (2020). Middle Miocene long-term continental temperature change in and out of pace with marine climate records. *Scientific Reports*, *10*, 7989. https://doi.org/10.1038/s41598-020-64743-5

Meybeck, M., Laroche, L., Dürr, H. H., & Syvitski, J. P. M. (2003). Global variability of daily total suspended solids and their fluxes in rivers. *Global and Planetary Change*, *39*, 65–93. https://doi.org/10.1016/S0921-8181(03)00018-3

Meyer-Peter, E., & Müller, R. (1948). Formulas for bed-load transport. In *Proceedings, 2nd Meeting, Int. Assoc. Hyddraul. Res. (IAHR)* (pp. 39–64) https://repository.tudelft.nl/islandora/object/uuid:4fda9b61-be28-4703-ab06-43cdc2a21bd7

Miller, K. L., Szabó, T., Jerolmack, D. J., & Domokos, G. (2014). Quantifying the significance of abrasion and selective transport for downstream fluvial grain size evolution. *Journal of Geophysical Research, F: Earth Surface*, *119*, 2412–2429. https://doi.org/10.1002/2014JF003156

Mohrig, D., Heller, P. L., & Lyons, W. J. (2000). Interpreting avulsion process from ancient alluvial sequences: Guadalope-Matarranya system (northern Spain) and Wasatch Formation (western Colorado). *Geological Society of America Bulletin*, *112*, 1787–1803. https://doi.org/10.1130/0016-7606(2000)112<1787:IAPFAA>2.0.CO;2

Molnar, P. (2001). Climate change, flooding in arid environments, and erosion rates. *Geology*, *29*(12), 1071–1074. https://doi.org/10.1130/0091-7613(2001)029<1071:CCFIAE>2.0.CO;2

Mosbrugger, V., Utescher, T., & Dilcher, D. L. (2005). Cenozoic continental climatic evolution of Central Europe. *Proceedings of the National Academy of Sciences of the United States of America*, *102*, 14964–14969. https://doi.org/10.1073/pnas.0505267102

Navratil, O., Albert, M.-B., Hérouin, E., & Gresillon, J.-M. (2006). Determination of bankfull discharge magnitude and frequency: Comparison of methods on 16 gravel-bed river reaches. *Earth Surface Processes and Landforms*, *31*, 1345–1363. https://doi.org/10.1002/esp

Paola, C., Heller, P. L., & Angevinet, C. L. (1992). The large scale dynamics of grain size variation in alluvial basins, 1: Theory. *Basin Research*, *4*, 73–90. https://doi.org/10.1111/j.1365-2117.1992.tb00145.x

Paola, C., & Mohrig, D. (1996). Palaeohydraulics revisited: Palaeoslope estimation in coarse-grained braided rivers. *Basin Research*, *8*, 243–254. https://doi.org/10.1046/j.1365-2117.1996.00253.x

Paola, C., & Voller, V. R. (2005). A generalized Exner equation for sediment mass balance. *Journal of Geophysical Research - Earth Surface*, *110*, 1–8. https://doi.org/10.1029/2004JF000274

Parker, G. (1978). Self-formed straight rivers with equilibrium banks and mobile bed. Part 2. The gravel river. *Journal of Fluid Mechanics*, *89*, 127–146. https://doi.org/10.1017/S0022112078002505

Parker, G. (1991). Selective sorting and abrasion of river gravel. I: Theory. *Journal of Hydraulic Engineering*, *117*, 131–147. https://doi.org/10.1061/(ASCE)0733-9429(1991)117:2(131)

Parker, G., Paola, C., Whipple, K. X., & Mohrig, D. (1998). Alluvial fans formed by channelized fluvial and sheet flow. I: Theory. *Journal of Hydraulic Engineering*, *124*, 985–995. https://doi.org/10.1061/(ASCE)0733-9429(1998)124:10(996)

Parker, G., & Toro-Escobar, C. M. (2002). Equal mobility of gravel in streams: The remains of the day. *Water Research*, *38*(11), 46-1–46-8. https://doi.org/10.1029/2001WR000669

Parker, G., Klingeman, P. C., & McLean, D. G. (1982). Bedload and size distribution in paved gravel-bed streams. *Journal of Hydraulics Division, ASCE*, *108*(HY4), 544–571. https://doi.org/10.1061/JYCEAJ.0005854

Parsons, A. J., Michael, N. A., Whittaker, A. C., Duller, R. A., & Allen, P. A. (2012). Grain-size trends reveal the late orogenic tectonic and erosional history of the south-central Pyrenees, Spain. *Journal of the Geological Society of London*, *169*, 111–114. https://doi.org/10.1144/0016-76492011-087

Pfeiffer, A. M., & Finnegan, N. J. (2018). Regional variation in gravel riverbed mobility, controlled by hydrologic regime and

sediment supply. *Geophysical Research Letters*, *45*, 3097–3106. https://doi.org/10.1002/2017GL076747

Pfiffner, O. A. (1986). Evolution of the north Alpine foreland basin in the Central Alps (Switzerland). *Foreland Basins*, *8*, 219–228. https://doi.org/10.1002/9781444303810.ch11

Pfiffner, O. A., Schlunegger, F., & Buiter, S. J. H. (2002). The Swiss Alps and their peripheral foreland basin: Stratigraphic response to deep crustal processes. *Tectonics*, *21*, 1–16. https://doi.org/10.1029/2000TC900039

Recking, A., Liébault, F., Peteuil, C., & Jolimet, T. (2012). Testing bedload transport equations with consideration of time scales. *Earth Surface Processes and Landforms*, *37*, 774–789. https://doi.org/10.1002/esp.3213

Rice, S. P. (1999). The nature and controls on downstream fining within sedimentary links. *Journal of Sedimentary Research*, *69*, 32–39. https://doi.org/10.2110/jsr.69.32

Rice, S. P., & Church, M. (1996). Sampling surficial fluvial gravels; the precision of size distribution percentile sediments. *Journal of Sedimentary Research*, *66*, 654–665. https://doi.org/10.2110/jsr.66.654

Romans, B. W., Castelltort, S., Covault, J. A., Fildani, A., & Walsh, J. P. (2016). Environmental signal propagation in sedimentary systems across timescales. *Earth Science Reviews*, *153*, 7–29. https://doi.org/10.1016/j.earscirev.2015.07.012

Sadler, P. M. (1981). Sediment accumulation rates and the completeness of stratigraphic sections. *Journal of Geology*, *89*, 569–584. www.jstor.com/stable/30062397

Schlunegger, F. (1999). Controls of surface erosion on the evolution of the Alps: Constraints from the stratigraphies of the adjacent foreland basins. *International Journal of Earth Sciences*, *88*, 285–304. https://doi.org/10.1007/s005310050265

Schlunegger, F., Burbank, D. W., Matter, A., Engesser, B., & Mödden, C. (1996). Magnetostratigraphic calibration of the Oligocence to middle Miocene (30–15 Ma) mammal biozones and depositional sequences of the Swiss Molasse Basin. *Eclogae Geologicae Helvetiae*, *89*, 753–788. https://doi.org/10.5169/seals-168650

Schlunegger, F., & Castelltort, S. (2016). Immediate and delayed signal of slab breakoff in Oligo/Miocene Molasse deposits from the European Alps. *Scientific Reports*, *6*, 31010. https://doi.org/10.1038/srep31010

Schlunegger, F., Delunel, R., & Garefalakis, P. (2020). Short communication: Field data reveal that the transport probability of clasts in Peruvian and Swiss streams mainly depends on the sorting of the grains. *Earth Surface Dynamics*, *8*, 717–728. https://doi.org/10.5194/esurf-8-717-2020

Schlunegger, F., Jordan, T. E., & Klaper, E. M. (1997). Controls of erosional denudation in the orogen on foreland basin evolution: The Oligocene central Swiss Molasse Basin as an example. *Tectonics*, *16*, 823–840. https://doi.org/10.1029/97TC01657

Schlunegger, F., & Kissling, E. (2015). Slab rollback orogeny in the Alps and evolution of the Swiss Molasse basin. *Nature Communications*, *6*, 8605. https://doi.org/10.1038/ncomms9605

Schlunegger, F., & Kissling, E. (2022). Slab load controls beneath the Alps on the source-to-sink sedimentary pathways in the Molasse Basin. *Geoscience*, *12*, 1–37. https://doi.org/10.3390/geosciences12060226

Schlunegger, F., Leu, W., & Matter, A. (1997). Sedimentary sequences, seismic facies, subsidence analysis, and evolution of the Burdigalian Upper Marine Molasse Group, central Switzerland. *AAPG Bulletin*, *81*, 1185–1207. https://doi.org/10.1306/522B4A19-1727-11D7-8645000102C1865D

Schlunegger, F., Matter, A., Burbank, D. W., & Klaper, E. M. (1997). Magnetostratigraphic constraints on relationships between evolution of the central Swiss Molasse basin and Alpine orogenic events. *GSA Bulletin*, *109*, 225–241. https://doi.org/10.1130/0016-7606(1997)109<0225:MCORBE>2.3.CO;2

Schlunegger, F., Matter, A., & Mange, M. A. (1993). Alluvial fan sedimentation and structure of the southern Molasse Basin margin, Lake Thun area, Switzerland. *Eclogae Geologicae Helvetiae*, *86*, 717–750. https://doi.org/10.5169/seals-167260

Schlunegger, F., Melzer, J., & Tucker, G. E. (2001). Climate, exposed source-rock lithologies, crustal uplift and surface erosion: A theoretical analysis calibrated with data from the Alps/North Alpine foreland basin system. *International Journal of Earth Sciences*, *90*, 484–499. https://doi.org/10.1007/s005310100174

Schlunegger, F., & Mosar, J. (2011). The last erosional stage of the Molasse Basin and the Alps. *International Journal of Earth Sciences*, *100*, 1147–1162. https://doi.org/10.1007/s00531-010-0607-1

Schlunegger, F., & Norton, K. P. (2013). Headward retreat of streams in the Late Oligocene to Early Miocene Swiss Alps. *Sedimentology*, *60*, 85–101. https://doi.org/10.1111/sed.12010

Schlunegger, F., Slingerland, R. L., & Matter, A. (1998). Crustal thickening and crustal extension as controls on the evolution of the drainage network of the central Swiss Alps between 30 Ma and the present: Constraints from the stratigraphy of the North Alpine Foreland Basin and the structural evolution of the. *Basin Research*, *10*, 197–212. https://doi.org/10.1046/j.1365-2117.1998.00063.x

Schlunegger, F., & Willett, S. D. (1999). Spatial and temporal variations in exhumation of the central Swiss Alps and implications for exhumation mechanisms. *Geological Society—Special Publications*, *154*, 157–179. https://doi.org/10.1144/GSL.SP.1999.154.01.07

Schmid, S. M., Pfiffner, O. A., Froitzheim, N., Schönborn, G., & Kissling, E. (1996). Geophysical-geological transect and tectonic evolution of the Swiss-Italian Alps. *Tectonics*, *15*, 1036–1064. https://doi.org/10.1029/96TC00433

Sharma, N., Whittaker, A. C., Adatte, T., & Castelltort, S. (2024). Water discharge and sediment flux intermittency in the fluvial Escanilla Formation, Spain: Implications for changes in stratigraphic architecture. *The Depositional Record*, *10*, 245–259. https://doi.org/10.1002/dep2.272

Shields, A. (1936). *Anwendung der Ähnlichkeitsmechanik und der Turbulenzforschung auf die Geschiebebewegung* (p. 26). Preuss. Versuchsanstalt für Wasserbau und Schiffbau.

Sinclair, H. D. (1997). Flysch to Molasse transition in peripheral foreland basins: The role of the passive margin versus slab breakoff. *Geology*, *25*, 1123–1126. https://doi.org/10.1130/0091-7613(1997)025<1123:FTMTIP>2.3.CO;2

Sinclair, H. D., Coakley, B. J., Allen, P. A., & Watts, A. B. (1991). Simulation of Foreland Basin stratigraphy using a diffusion model of Mountain Belt uplift and erosion: An example from the Central Alps, Switzerland. *Tectonics*, *10*, 599–620. https://doi.org/10.1029/90TC02507

Sinclair, H. D., & Naylor, M. (2012). Foreland basin subsidence driven by topographic growth versus plate subduction. *Bulletin Geological Society of America*, *124*, 368–379. https://doi.org/10.1130/B30383.1

Sissingh, W. (1997). Tectonostratigraphy of the North Alpine Foreland Basin: Correlation of tertiary depositional cycles and orogenic phases. *Tectonophysics*, *282*, 223–256. https://doi.org/10.1016/S0040-1951(97)00221-7

Spiegel, C., Kuhlemann, J., Dunkl, I., & Frisch, W. (2001). Paleogeography and catchment evolution in a mobile orogenic belt: The Central Alps in Oligo-Miocene times. *Tectonophysics*, *341*, 33–47. https://doi.org/10.1016/S0040-1951(01)00187-1

Spiegel, C., Kuhlemann, J., Dunkl, I., Frisch, W., & Eynatten, H. V. (2000). The erosion history of the Central Alps: Evidence from zircon fission track data of the foreland basin sediments. *Terra Nova*, *12*, 163–170. https://doi.org/10.1046/j.1365-3121.2000.00289.x

Stürm, B. (1973). *Die Rigi Schüttung – Sedimentpetrographie, Sedimentologie, Palaeogeographie, Tektonik* (Unpublished PhD thesis, p. 96). University of Bern.

Steck, A., Della Torre, F., Keller, F., Pfeifer, H. R., Hunziker, J., & Masson, H. (2013). Tectonics of the Lepontine Alps: Ductile thrusting and folding in the deepest tectonic levels of the Central Alps. *Swiss Journal of Geosciences*, *106*, 427–450. https://doi.org/10.1007/s00015-013-0135-7

Sternberg, H. (1875). Untersuchungen über Längen- und Querprofil geschiebeführender Flüsse. *Zeitschrift für Bauwes.*, *25*, 483–506. (in German). https://digital.zlb.de/viewer/image/15239363_1875/262/

Stock, J. D., Schmidt, K. M., & Miller, D. M. (2008). Controls on alluvial fan long-profiles. *Bulletin Geological Society of America*, *120*, 619–640. https://doi.org/10.1130/B26208.1

Strasky, S., Schlunegger, F., Hänni, R., Häuselmann, P., Mojon, A., & Schwizer, B. (2022). Blatt 1208 Beatenberg—Geologischer Atlas der Schweiz 1: 25 000. Erläut. 170–171. www.swisstopo.ch

Straub, K. M., Duller, R. A., Foreman, B. Z., & Hajek, E. A. (2020). Buffered, incomplete, and shredded: The challenges of reading an imperfect stratigraphic record. *Journal of Geophysical Research: Earth Surface*, *125*, 1–44. https://doi.org/10.1029/2019JF005079

Stutenbecker, L., Tollan, P. M. E., Madella, A., & Lanari, P. (2019). Miocene basement exhumation in the Central Alps recorded by detrital garnet geochemistry in foreland basin deposits. *Solid Earth*, *10*, 1581–1595. https://doi.org/10.5194/se-2019-98

Tanner, H. J. (1944). Beitrag zur Geologie der Molasse zwischen Ricken und Hörnli. *Mitteilungen der Thurgauischen Naturforschenden Gesellschaft*, *33*, 1–108. https://doi.org/10.5169/seals-593971

Tucker, G. E., & Slingerland, R. L. (1997). Drainage basin responses to climate change. *Water Resources Research*, *33*, 2031–2047. https://doi.org/10.1029/97WR00409

van der Boon, A., Beniest, A., Ciurej, A., Gaździcka, E., Grothe, A., Sachsenhofer, R. F., Langereis, C. G., & Krijgsman, W. (2018). The Eocene–Oligocene transition in the North Alpine Foreland Basin and subsequent closure of a Paratethys gateway. *Global and Planetary Change*, *162*, 101–119. https://doi.org/10.1016/j.gloplacha.2017.12.009

Ventra, D., & Clarke, L. E. (2018). Geology and geomorphology of alluvial and fluvial fans: Current progress and research perspectives. *Special Publication. Geological Society of London*, *440*, 1–21. https://doi.org/10.1144/sp440.16

Ventra, D., & Nichols, G. J. (2014). Autogenic dynamics of alluvial fans in endorheic basins: Outcrop examples and stratigraphic significance. *Sedimentology*, *61*, 767–791. https://doi.org/10.1111/sed.12077

Wainwright, J., Parsons, A. J., Cooper, J. R., Gao, P., Gillies, J. A., Mao, L., Orford, J. D., & Knight, P. G. (2015). The concept of transport capacity in geomorphology. *Reviews of Geophysics*, *53*, 1155–1202. https://doi.org/10.1002/2014RG000474

Whittaker, A. C. (2012). How do landscapes record tectonics and climate? *Lithosphere*, *4*, 160–164. https://doi.org/10.1130/RF.L003.1

Whittaker, A. C., Duller, R. A., Springett, J., Smithells, R. A., Whitchurch, A. L., & Allen, P. A. (2011). Decoding downstream trends in stratigraphic grain size as a function of tectonic subsidence and sediment supply, *123*, 1363–1382. https://doi.org/10.1130/B30351.1

Wickert, A. D., & Schildgen, T. F. (2019). Long-profile evolution of transport-limited gravel-bed rivers. *Earth Surface Dynamics*, *7*, 17–43. https://doi.org/10.5194/esurf-7-17-2019

Wolman, M. G. (1954). A method of sampling coarse river-bed material. *Transactions of the American Geophysical Union*, *35*, 951–956. https://doi.org/10.1029/TR035i006p00951

Wong, M., & Parker, G. (2006). Reanalysis and correction of bed-load relation of Meyer-Peter and Müller using their own database. *Journal of Hydraulic Engineering*, *132*, 1159–1168. https://doi.org/10.1061/(asce)0733-9429(2006)132:11(1159)

Zachos, J. C., Pagani, H., Sloan, L., Thomas, E., & Billups, K. (2001). Trends, rhythms, and aberrations in global climate 65 Ma to present. *Science (80)*, *292*, 686–693. https://doi.org/10.1126/science.1059412

SUPPORTING INFORMATION

Additional supporting information can be found online in the Supporting Information section at the end of this article.

How to cite this article: Garefalakis, P., do Prado, A. H., Whittaker, A. C., Mair, D., & Schlunegger, F. (2024). Quantification of sediment fluxes and intermittencies from Oligo–Miocene megafan deposits in the Swiss Molasse basin. *Basin Research*, *36*, e12865. https://doi.org/10.1111/bre.12865